The Astrophysical Journal Letters, 955:L21 (19pp), 2023 September 20 https://doi.org/10.3847/2041-8213/acec70

X-Ray Detection of the Galaxy's Missing Baryons in the Circumgalactic Medium of L^* Galaxies

Fabrizio Nicastro[1,2], Y. Krongold[3], T. Fang[2], F. Fraternali[4], S. Mathur[5,6], S. Bianchi[7], A. De Rosa[8], E. Piconcelli[1], L. Zappacosta[1], M. Bischetti[9,10], C. Feruglio[9], A. Gupta[5,11], and Z. Zhou[2]
[1] Istituto Nazionale di Astrofisica (INAF)—Osservatorio Astronomico di Roma Via Frascati, 33 I-00078 Monte Porzio Catone (RM), Italy; fabrizio.nicastro@inaf.it
[2] Department of Astronomy, Xiamen University, Xiamen, Fujian 361005, People's Republic of China
[3] Instituto de Astronomia—Universidad Nacional Autonoma de Mexico, Mexico City, Mexico
[4] Kapteyn Astronomical Institute, University of Gronigen, Gronigen, The Netherlands
[5] Astronomy Department, The Ohio State University, Columbus, OH, USA
[6] Center for Cosmology and Astro-Particle Physics, The Ohio State University, Columbus, OH, USA
[7] Dipartimento di Matematica e Fisica, Universitá degli Studi Roma Tre, Roma, Italy
[8] Istituto Nazionale di Astrofisica (INAF)—Istituto di Astrofisica e Planetologia Spaziali, Roma, Italy
[9] Istituto Nazionale di Astrofisica (INAF)—Osservatorio Astronomico di Trieste, Trieste, Italy
[10] Dipartimento di Fisica, Sezione di Astronomia, Universitá di Trieste, Trieste, Italy
[11] Columbus State Community College, Columbus, OH, USA
Received 2023 February 8; revised 2023 July 26; accepted 2023 July 29; published 2023 September 25

Abstract

The number of baryons hosted in the disks of galaxies is lower than expected based on the mass of their dark matter halos and the fraction of baryon-to-total matter in the Universe, giving rise to the so-called galaxy missing-baryon problem. The presence of cool circumgalactic matter gravitationally bound to its galaxy's halo up to distances of at least 10 times the size of the galaxy's disk mitigates the problem but is far from being sufficient for its solution. It has instead been suggested that the galaxy's missing baryons may hide in a much hotter gaseous phase of the circumgalactic medium, possibly near the halo virial temperature and coexisting with the cool phase. Here we exploit the best available X-ray spectra of known cool circumgalactic absorbers of L^* galaxies to report the first direct high statistical significance (best estimates ranging from 4.2σ to 5.6σ, depending on fitting methodology) detection of associated O VII absorption in the stacked XMM-Newton and Chandra spectra of three quasars. We show that these absorbers trace the hot medium in the X-ray halo of these systems at $\log T(\mathrm{in\ K}) \simeq 5.8$–$6.3$ (comprising the halo virial temperature $T_{\rm vir} \simeq 10^6$ K). We estimate masses of the X-ray halo within one virial radius within the interval $M_{\rm hot-CGM} \simeq (1\text{–}1.7) \times 10^{11} (Z/0.3Z_\odot)^{-1}\ M_\odot$. For these systems, this corresponds to galaxy missing-baryon fractions in the range $\xi_b = M_{\rm hot-CGM}/M_{\rm missing} \simeq (0.7\text{–}1.2)(Z/0.3Z_\odot)^{-1}$, thus potentially closing the galaxy baryon census in typical L^* galaxies. Our measurements contribute significantly to the solution of the long-standing galaxy missing-baryon problem and to the understanding of the continuous cycle of baryons in-and-out of galaxies throughout the life of the Universe.

Unified Astronomy Thesaurus concepts: Circumgalactic medium (1879); Missing mass (1068); X-ray astronomy (1810); Galaxies (573); Lyman limit systems (981); Quasar absorption line spectroscopy (1317)

1. Introduction

The galaxy missing-baryon problem is present at all halo scales, from dwarfs to massive elliptical galaxies and up to groups and clusters of galaxies (e.g., McGaugh et al. 2010), but the baryon deficit is larger for smaller halos. Galaxy disks in halos of $10^{12}\ M_\odot$ host only ∼20% of the expected baryons (McGaugh et al. 2010). However, due to their nonbaryonic massive halos, the gravitational pull of galaxies extends well beyond their stellar disks, up to distances of at least 10 times their size.

Such large volumes of space surrounding the stellar disks are not empty but are known to host clouds of cool ($T \simeq 10^4$ K) gas gravitationally bound to the galaxy. As suggested by the extensive studies carried out for the local Universe in the far-ultraviolet (FUV) band (∼900–2000 Å) with the Hubble Cosmic Origin Spectrograph (COS; McPhate et al. 2000), this cool circumgalactic matter (cool CGM) may be in photoionization equilibrium with the external metagalactic UV radiation field in which it is embedded (e.g., Fox et al. 2013; Lehner et al. 2013, 2018, 2019; Stocke et al. 2013; Werk et al. 2013, 2014; Keeney et al. 2017; Berg et al. 2019, 2023; Wotta et al. 2019, but see also Bregman et al. 2018 and references therein for alternative possibilities) and often coexists with higher-ionization gas in a different physical state probed by Li-like ions of oxygen (e.g., Prochaska et al. 2011; Stocke et al. 2013; Prochaska et al. 2019; Tchernyshyov et al. 2022) and/or neon (e.g., Burchett et al. 2019). Under the pure photoionization equilibrium hypothesis, the cool CGM may contribute importantly to the galaxy baryon budget; for typical L^* galaxies[12] with a halo mass of $1.6 \times 10^{12}\ M_\odot$ and a factor of 4 deficit of baryons (e.g., McGaugh et al. 2010), it may account for up to 50% of the missing baryonic matter (Werk et al. 2014; but see also Bregman et al. 2018).

At least 50% of the galaxy's missing baryons, however, remain elusive and are thought to hide in a hotter phase of the

[12] Here L^* is the characteristic luminosity above which the number of galaxies per unit volume drops exponentially and, in the local Universe, corresponds to the luminosity of a Milky Way–like galaxy.

CGM (Wijers et al. 2020), possibly at the galaxy virial temperature (i.e., $T_{\rm vir} \simeq 10^{5.7–6.0}$ K for halo masses of $M_h \simeq 10^{11.8–12.3}$ $M_\odot$ at $z = 0$; e.g., Qu & Bregman 2018). Observationally, the presence of this hot phase is currently only hinted at through Sunyaev–Zel'dovich (Bregman et al. 2022) and low-resolution X-ray (Das et al. 2020) measurements of the surroundings of local L^* galaxies or pioneering X-ray absorption (Mathur et al. 2021) studies (see below) and, more ubiquitously, through absorption by moderately ionized ions of oxygen (e.g., Prochaska et al. 2011; Stocke et al. 2013; Prochaska et al. 2019; Tchernyshyov et al. 2022) and neon (e.g., Burchett et al. 2019). At such high temperatures, indeed, hydrogen is virtually fully ionized and thus difficult to detect. Therefore, the only available tracers (with typical ion fractions of only a few percent) in the FUV portion of the electromagnetic spectrum are the Li-like ions of oxygen (at $z \leqslant 0.7$) and neon (at $z \simeq 0.2–1.3$). However, Li-like ions in the CGM may be produced either in tenuous warm clouds purely photoionized by the external radiation field or in much hotter, mainly collisionally ionized, gas (see Appendix D). Distinguishing between these two possibilities is virtually impossible based on the currently available single ion column density measurements (i.e., without estimates of the gas ionization balance); thus, only loose lower limits on the temperature and mass contribution of this gaseous CGM component have been set so far (e.g., Chen & Prochaska 2000; Tumlinson et al. 2011).

A better tracer of gas at $T \simeq 10^6$ K is the He-like ion of oxygen, which represents about 90%–99% of its element in $T \simeq 10^{5.6–6.2}$ K gas in collisional–ionization equilibrium (CIE; see Appendix D) and whose main transitions lie in the soft X-ray band. Pioneering single-target X-ray spectroscopic studies of these transitions from the halos of optimally selected Lyman-limit systems (LLSs; low-ionization H I metal absorbers with moderate column density $16.2 \leqslant \log N_{\rm H\,I}({\rm in\ cm^{-2}}) \leqslant 19$) have indeed been recently performed (Mathur et al. 2021) but were hampered by the limited resolution and throughput of current X-ray spectrometers and did not produce conclusive results. Detailed surveys of associations between galaxies and intervening high-ionization X-ray absorbers, comparable to low- or moderate-ionization FUV studies like the COS-Halos Survey (Werk et al. 2013) or the CGM2 Survey (Tchernyshyov et al. 2022), will have to wait for the next generation of high-throughput X-ray spectrometers (e.g., the Athena-XIFU, Barret et al. 2018; or Arcus, Smith 2020; Wijers et al. 2020). In the meantime, exploiting the richness of the Chandra Low Energy Transmission Grating (LETG; Brinkman et al. 2000) and XMM-Newton Reflection Grating Spectrometers (RGS; den Herder et al. 2000) archives and adopting "stacking" techniques (e.g., Kovács et al. 2019; Ahoranta et al. 2020, 2021) to perform spectroscopy of optimally selected targets is a viable alternative.

Previous studies pursued this strategy by using as signposts for the X-ray transitions the average redshifts of groups of intervening galaxies and reported nondetection of hot X-ray intragroup gas (Yao et al. 2010). Here, instead, we choose to focus on the redshifts of known intervening cool (LLSs) and warm absorbers already extensively studied in the FUV and their galaxy associations.

Throughout the paper, we adopt a standard ΛCDM cosmology with the latest parameter values from Planck Collaboration et al. (2020; from the combined analysis of temperature power spectra, high-multipole polarization spectra, and lensing). In particular, we use the universal baryon fraction $f_b = \Omega_b/\Omega_m = 0.157$ (baryon over total matter). We also adopt solar metallicities from Anders & Grevesse (1989). In particular, we use $[{\rm O/H}] = -3.07$. Uncertainties are quoted at 68% significance (for one interesting parameter throughout the paper, unless explicitly stated). Analogously, line equivalent width (EW) versus centroid wavelength statistical significance contours are displayed for $\Delta\chi^2 = n^2$ ($n = 1$, 2, 3, 4, 5, ...) for easy comparison with the statistical significance of the line evaluated as the ratio between the line EW and its 1σ statistical uncertainty. These $\Delta\chi^2$ correspond to (1, 2, 3, 4, 5, ...)σ contours for one interesting parameter (the line EW) and $\simeq$ (0.5, 1.4, 2.6, 3.7, 4.7, ...)σ for two interesting parameters (line EW and centroid). All spectral fitting is performed with the fitting package *Sherpa* (part of the CIAO software; Fruscione et al. 2006) by exploiting χ^2 statistics. We look for minima using two consecutive methods: the *levmar* method in *Sherpa* (Moré 1978) to look for quick solutions, followed by a second fit with the slower *moncar* method in *Sherpa* (Storn & Price 1997) to refine the best-fitting parameters or look for alternative solutions.

2. Sample Selection and the X-Ray Halo

We select as optimal targets the 30 background quasars of Lehner et al. (2013) and Prochaska et al. (2019) for which LLSs are reported, often associated with moderate-ionization O VI absorbers (Fox et al. 2013; Lehner et al. 2013).

Eleven of these objects have XMM-Newton RGS data available, and two also have Chandra LETG data (see Appendix A). Of these 11 targets, we selected only those (a) whose intervening LLSs have been confidently associated with $\sim L^*$ galaxies and, among those, (b) the ones whose total RGS and LETG spectra have a signal-to-noise ratio per resolution element (SNRE) of >4 in the continuum adjacent to the LLS frame O VII Kα transition. The second of these two selection criteria allows for the search of associated O VII $_{\rm K\alpha}$ absorption in the individual X-ray spectra of the targets (see Appendix A for additional details).

This yielded three quasars, namely, PG 1407+265 (observed only with XMM-Newton), PKS 0405−123, and PG 1116+215 (observed with both XMM-Newton and Chandra), whose lines of sight cross low-ionization LLSs and O VI absorbers at $z_{\rm LLS\ 1} = 0.6828$ (LLS 1; Fox et al. 2013; Lehner et al. 2013; Wotta et al. 2019), $z_{\rm LLS\ 2} = 0.1671$ (LLS 2; Fox et al. 2013; Lehner et al. 2013; Stocke et al. 2013; Wotta et al. 2019), and $z_{\rm LLS\ 3} = 0.1385$ (LLS 3; Fox et al. 2013; Lehner et al. 2013; Stocke et al. 2013; Wotta et al. 2019), respectively (see Appendix A).

The three LLSs that we use to build our X-ray halo and their galaxy associations have been reported and discussed in several studies (Fox et al. 2013; Lehner et al. 2013; Stocke et al. 2013; Werk et al. 2013; Keeney et al. 2017; Burchett et al. 2019; Wotta et al. 2019; Berg et al. 2023), and their properties are reported in Table 5 of Appendix B. They all have H I column densities close to the lowest threshold, $N_{\rm H\,I} = 10^{16.2}$ cm^{-2}, of the LLS definition in Lehner et al. (2013) and are seen at impact parameters (i.e., the line of sight to the galaxy center projected distance) of $\rho > 90$ kpc (Table 5 in Appendix B). This strongly suggests a cool CGM (and not an extended gaseous disk) origin for the H I metal absorbers observed in these three systems (Bregman et al. 2018). The three LLSs of our sample also have colocated O VI absorption that, however, in the pure photoionization hypothesis for the cool CGM traced

Table 1
Best-fitting Parameters of the X-Ray Halo Lines in the Single Spectra of the Three Targets

X-Ray Spectrum	$\lambda^{\rm OVII\ K\alpha}_{\rm LLS\ frame}$ (Å)	$EW^{\rm OVII\ K\alpha}_{\rm LLS\ frame}$ (mÅ)	Δv (km s^{-1})	Significance
Fits to Individual Spectra				
1: PG 1407+265 RGS	21.59 ± 0.03	59 ± 35	$-(140 \pm 420)$	1.7σ
2: PKS 0405−123 RGS	21.54 ± 0.03	15.7 ± 7.1	$-(830 \pm 420)$	2.2σ
3: PKS 0405−123 LETG	21.57 ± 0.05	69 ± 25	$-(420 \pm 690)$	2.8σ
4: PG 1116+215 RGS	21.54 ± 0.03	20.8 ± 8.0	$-(830 \pm 420)$	2.6σ
5: PG 1116+215 LETG	21.48 ± 0.05	29.0 ± 14.5	$-(1670 \pm 690)$	2.0σ
Joint Fits to RGS+LETG Spectra with EWs Linked to the Same Value				
PKS 0405−123 RGS+LETG	21.56 ± 0.04	20.5 ± 7.3	$-(560 \pm 560)$	2.8σ
PG 1116+215 RGS+LETG	21.51 ± 0.04	18.1 ± 6.5	$-(1250 \pm 560)$	2.8σ
Weighted Averages and Coadded Significance				
X-ray halo	21.55 ± 0.04	28.5 ± 6.6	$-(690 \pm 560)$	4.3

by the LLSs, cannot be entirely physically associated with the cool gas (e.g., Lehner et al. 2013).

The X-ray halo resulting from the $\sigma^i_{\rm OVII}$-weighted averages (see Section 3 and Appendix B) of the properties of the LLSs and galaxy associations of our sample is that of an L^* galaxy at $\langle z_{\rm X\text{-}ray-halo}\rangle = 0.276$, with a halo mass of $\langle M_h\rangle \simeq 1.2 \times 10^{12}\ M_\odot$ and a virial radius of $\langle R_{\rm vir}\rangle = R_{200} \simeq 195$ kpc (the radius at which the halo density equals 200× the Universe's critical density at the given redshift). The constructed X-ray line of sight intercepts the X-ray halo at a projected distance of $\langle\rho\rangle = 115$ kpc from its center ($\sim 0.6\ \langle R_{\rm vir}\rangle$; last row of Table 5 in Appendix B). Assuming a spherical halo with a virial radius of $\langle R_{\rm vir}\rangle$, the line-of-sight path length through the X-ray halo is $L = 2\sqrt{\langle R_{\rm vir}\rangle^2 - \langle\rho\rangle^2} \simeq 315$ kpc.

3. The X-Ray Halo Spectrum

Table 4 of Appendix A lists the three targets of our X-ray halo sample and the properties of their X-ray spectra. The last row of Table 4 contains the total available X-ray exposure and SNRE (added in quadrature).

3.1. O VII Kα Absorption along Individual Sight Lines

We first examined each source's X-ray spectrum for a signature of O VII Kα absorption (the strongest transition expected in gas at $T \simeq 10^6$ K) at the redshift of its LLS. We did this by first modeling each RGS and LETG spectrum within the fitting package *Sherpa* with the simplest possible astrophysically motivated continuum model, i.e., a single power law plus Galactic absorption (the *xstbabs* model in *Sherpa*, which includes high-resolution edge structures for the *K* edges of oxygen and neon and the *L* edges of iron). In all cases, a visual inspection of the residuals showed broadband systematic wiggles, indicating that the single power-law model is not an adequate description of the targets' continua. We then added an *n*th-order polynomial function to the power law with all $n > 2$ coefficients initially frozen to zero and refitted the data. We iterated the procedure by gradually freeing $n > 2$ polynomial orders until the residuals appeared flat over the whole RGS and LETG 5–37 Å (observed) bands. Finally, to search for O VII Kα absorption at the redshift of the LLS, we added a negative unresolved (FWHM frozen to 10 mÅ) Gaussian to our best-fitting continuum models, with the position allowed to vary within 1 Å from its expected position at the LLS's redshift and free negative-only amplitude.

Table 1 summarizes the best-fitting line parameters, as derived by both fitting the individual spectra (first part of the Table) and joint fitting the RGS and LETG spectra of the same targets by linking their line EWs to the same value (rows 6 and 7 of the Table, where the line centroids are the $\sigma^i_{\rm OVII}$-weighted averages of the line centroids in the RGS and LETG spectra of the targets). Errors associated with line centroids are Gaussian-equivalent 1σ uncertainties (i.e., FWHM/$(2\sqrt{2\ln 2})$ derived from the distributions of the offsets of known Galactic lines in two samples of RGS and High Resolution Camera (HRC) LETG spectra (see Figure 9 in Appendix C), while errors on EWs are 1σ statistical errors from the data. The last row of the table reports the weighted-average line parameters for the X-ray halos, computed by adopting as weights the statistical significance $\sigma^i_{\rm OVII}$ ($i = 1, 3$) of the lines in the RGS spectrum of PG 1407+265 (first row of the Table) and the jointly fitted RGS+LETG spectra of PKS 0405−123 and PG 1116+215 (rows 6 and 7 of the table). The statistical significance of the X-ray halo O VII Kα line is the sum, in quadrature, of the line significance in those three spectra and is used to derive the 1σ error on the weighted-average EW.

Finally, Figure 1 shows the confidence-level contours of the LLS frame O VII Kα line EW and centroid seen in the individual XMM-Newton RGS and Chandra LETG spectra of our three targets (see the caption for details).

In summary, none of the single-source spectra shows the clear presence of a possible O VII Kα absorption line imprinted by the halo of the intervening galaxies, but all of them are consistent with the presence of such a feature at statistical significance levels between $\sigma^i_{\rm OVII} \sim 1.7$ and 2.8 ($i = 1, 5$). The line hinted at in the LETG spectrum of PKS 0405−123 was already reported by our group (Mathur et al. 2021) at the level of statistical significance also shown here in the middle panel of Figure 1 ($\sim 2\sigma$; dashed contours) and modeled as the hot counterpart of LLS 2 in association with the O VI absorber reported by Savage et al. (2010). However, the statistical significance of this line alone did not allow us to reach definitive conclusions on the temperature, column density, and mass of this hot CGM absorber (Mathur et al. 2021).

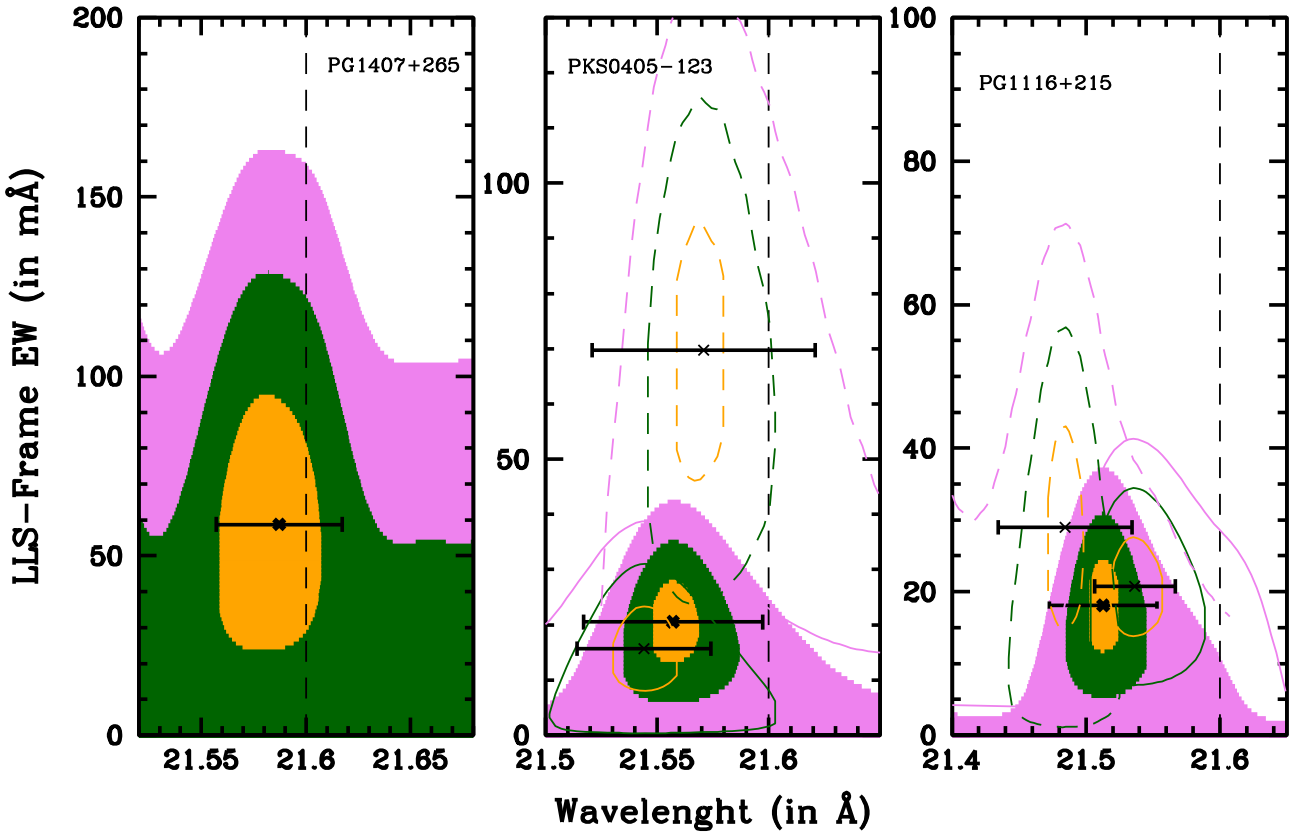

Figure 1. The 1σ (orange), 2σ (green), and 3σ (violet) confidence-level contours of the LLS frame O VII Kα line EW and centroid hinted at in the individual XMM-Newton RGS and Chandra LETG spectra of our three targets. Colored shaded areas are the EW-λ confidence levels for the best-fitting line parameters of the three LLSs in the RGS spectrum of PG 1407+265 (left panel) and the simultaneous RGS+LETG spectra of PKS 0405−123 (middle panel) and PG 1116+215 (right panel). Solid and dashed curves in the middle and right panels are the confidence-level best-fitting line parameters in the individual RGS and LETG spectra of PKS 0405−123 and PG 1116+215, respectively. Horizontal error bars are the 1σ uncertainties on the X-ray halo line centroids, evaluated as the Gaussian-equivalent standard deviations of the distributions of Figure 9 in Appendix C.

3.2. Simultaneous Fit to the O VII Absorbers of the Three LLSs

After checking for the presence of X-ray halo O VII Kα lines in the single XMM-Newton and Chandra spectra of our targets, we proceeded to simultaneously fit the five X-ray spectra of our sample in the common observed 5–37 Å band, with the same models used to model the single spectra independently (with continuum parameters frozen to their best-fitting values), plus the addition of a second negative and unresolved Gaussian with a position linked to that of the first Gaussian through the relative rest-frame positions of the O VII Kα and Kβ transitions, i.e., $\lambda^{\rm O\ VII\ K\beta} = \lambda^{\rm O\ VII K\alpha} \times (18.63/21.6)$.[13] We did this by exploiting three different methods, namely, (A) leaving all of the O VII Kα line positions and EWs and the O VII Kβ EWs free to vary independently in each spectrum, (B) same as method A but linking the Kα and Kβ line EWs of the RGS and LETG spectra of the same background targets (PKS 0405−123 and PG 1116+215) to the same values (as expected if the lines are due to intervening hot CGM), and (C) same as method B but also linking the line centroids of the RGS and LETG spectra of the same background targets (PKS 0405−123 and PG 1116+215) to the same values (probably too strong a requirement, given the breadth of the distributions of Figure 9 in Appendix C).

For each of these methods, A, B, and C, the best-fitting line parameters are listed in Table 2, and the line EW-position confidence-level contours are plotted in Figure 2. Finally, the raw RGS and LETG data of our targets, together with their best-fitting models for methods A (orange solid line), B (green solid line), and C (cyan solid line), are shown in Figure 3.

Uncertainties and confidence-level contours are computed by linking the line centroids and EWs to those of one of the spectra used as reference. In particular, we link the O VII Kα line positions of spectra 2–5 to that of spectrum 1 via the relations $\lambda_i^{\rm OVIIK\alpha} = \lambda_1^{\rm OVIIK\alpha} \times (\lambda_{{\rm bf},i}^{\rm OVIIK\alpha} / \lambda_{{\rm bf},1}^{\rm OVII})$ (where the index $i = 2,\ 5$ indicates the ith spectrum, and bf stands for best-fitting). Similarly, the fluxes F_i of each O VII Kα and Kβ line in spectra 2–5 are linked to $F_1^{\rm K\alpha,K\beta}$ through the relations $F_i^{\rm K\alpha,K\beta} = F_1^{\rm K\alpha,K\beta} \times (F_{{\rm bf},i}^{\rm K\alpha,K\beta} / F_{{\rm bf},1}^{\rm K\alpha,K\beta})$. This allows us to compute statistical errors on the flux of the O VII Kα and Kβ lines, leaving only three parameters (namely, the O VII Kα line centroid and Kα and Kβ fluxes of spectrum 1) free to vary independently and thus exploiting the combined statistics of all data. Finally, to compute the line position–EW confidence levels of the X-ray halo (i.e., O VII Kα+Kβ lines) absorbers plotted in Figure 2, we also link the flux of the Kβ line of the reference spectrum 1 to that of its corresponding Kα transition via the relation $F_1^{\rm OVIIK\beta} = F_1^{\rm OVIIK\alpha} \times (F_{{\rm bf},1}^{\rm OVIIK\beta} / F_{{\rm bf},1}^{\rm OVIIK\alpha})$, so that the confidence levels shown in Figure 2 are for the combined

[13] As shown in Appendix C (i.e., Figure 10), linking the positions of Kα and Kβ to their expected rest-frame ratio is extremely conservative for both the LETG and the RGS but allows for a closer comparison of the simultaneous fit to the individual spectra with that performed on the stacked spectrum obtained by rigidly shifting the individual X-ray spectra to either the X-ray– or FUV–LLS redshifts (see Section 3.3).

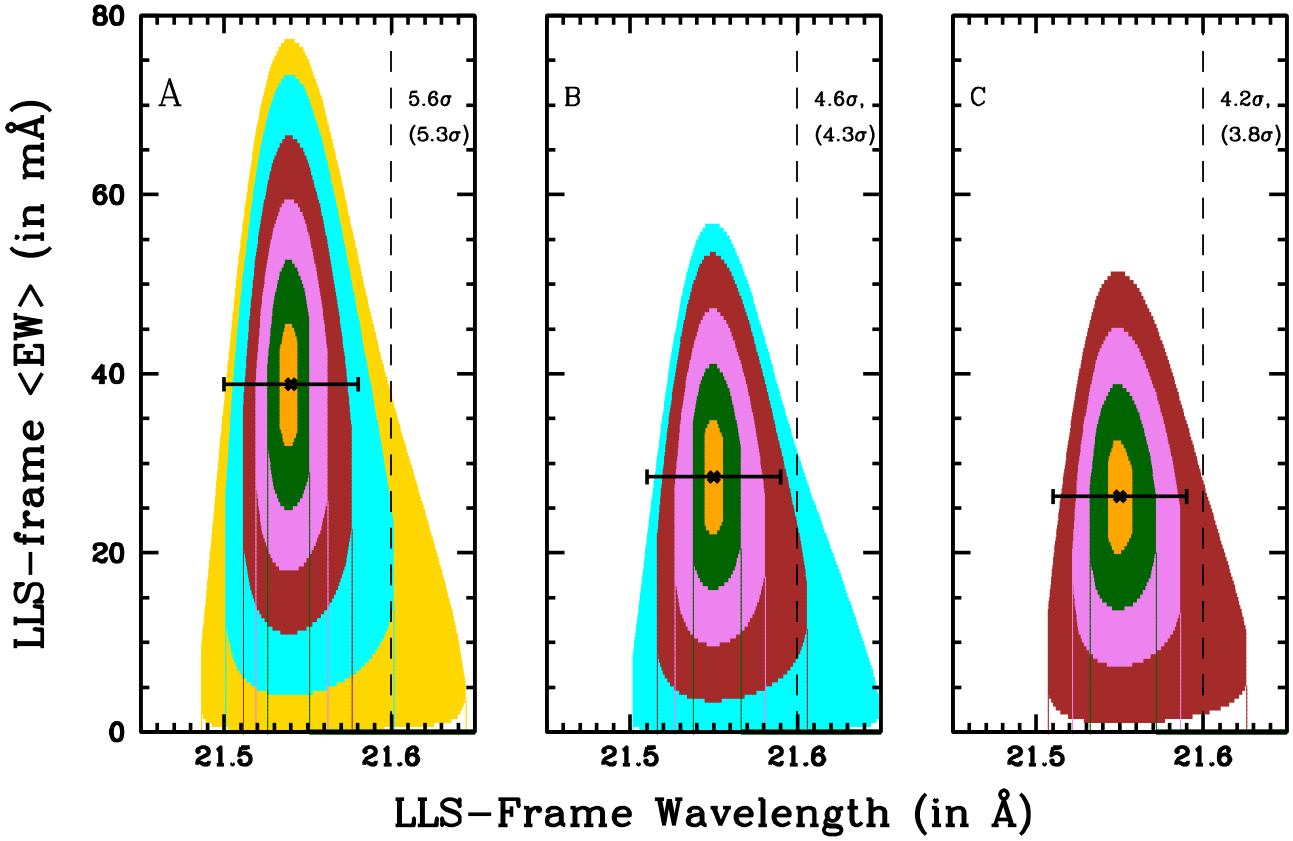

Figure 2. The O VII Kα+Kβ line EW-position confidence-level contours, up to the highest closed contour level, in the simultaneous fit to the five X-ray spectra of our X-ray halo sample. The three panels refer to the three different fitting methods described in the text, and for each method, the statistical significance of the highest closed contour is labeled for both one and two interesting parameters.

Table 2
Best-fitting Parameters of the X-Ray Halo Absorption Lines from the Simultaneous Fits

Method	$\langle\lambda^{\rm OVII\ K\alpha}_{\rm LLS_G-frame}\rangle$ (Å)	$\langle\lambda^{\rm OVII\ K\beta}_{\rm LLS_G-frame}\rangle$ (Å)	$\langle{\rm EW}^{\rm OVII\ K\alpha}_{\rm LLS_G-frame}\rangle$ (mÅ)	$\langle{\rm EW}^{\rm OVII\ K\beta}_{\rm LLS_G-frame}\rangle$ (mÅ)	Δv km s^{-1}	Significance of the X-Ray Halo
A	21.54 ± 0.04	18.58[a]	39.1 ± 7.4	9.4 ± 5.2	$-(830 \pm 560)$	5.6σ
B	21.55 ± 0.04	18.59[a]	28.5 ± 6.7	16.4 ± 10.3	$-(690 \pm 560)$	4.6σ
C	21.55 ± 0.04	18.59[a]	26.4 ± 7.1	17.3 ± 8.7	$-(690 \pm 560$	4.2σ

Note.
[a] Linked to the Kα position through the ratio of the rest-frame line positions.

O VII Kα and Kβ transitions. For each of the three cases, the values reported in Table 2 for the line centroids and EWs of the two transitions are the $\sigma^i_{\rm OVII}$-weighted averages of their best-fitting values in each spectrum (Table 1), while the statistical significance of the X-ray halo is the coadded (in quadrature) statistical significance of the O VII Kα and Kβ lines (which, by construction, coincides with that of the corresponding highest-significance closed contour of Figure 2).

3.3. Stacked Spectrum of the X-Ray Halo

Finally, to fully exploit the whole statistics of the five data sets in a single spectrum (combined with the lowest possible number of degrees of freedom), we proceeded to blueshift the five background-subtracted spectra and their best-fitting continuum models to both their own X-ray–LLS redshifts (i.e., the redshift derived from the best-fitting position of the O VII Kα lines in each spectrum, hereafter X-ray–LLS spectrum) and the exact FUV–LLS redshifts (i.e., the redshifts of the cool CGM absorbers in the HST-COS spectra of the three targets, hereafter FUV–LLS spectrum), regrid them over a common $\lambda_{\rm RF} = 1$–30 Å (where RF stands for rest frame) wavelength grid with a bin size of 30 mÅ (about 0.4 and 0.6 times the RGS and LETG line-spread function (LSF) FWHMs, respectively), and stack them together by weighting each spectrum and best-fitting continuum model by its relative signal-to-noise ratio per bin. Errors on the stacked raw counts per bin were computed in the Poissonian hypothesis (justified by the SNRE > 4 in the individual X-ray spectra of the targets of our sample) as $1 + \sqrt{0.75 + {\rm COUNTS}}$ (Gehrels 1986). We then ratioed the stacked spectra and their errors with their best-fitting continua to produce the final background-subtracted and continuum-normalized stacked spectra of the X-ray halo.

Strong absorption line–like signals are revealed at (left panels of Figure 4) or near (right panels of Figure 4) the rest-frame wavelengths of the strongest Kα and Kβ transitions of the He-like ion of oxygen in both the X-ray–LLS (left panels)

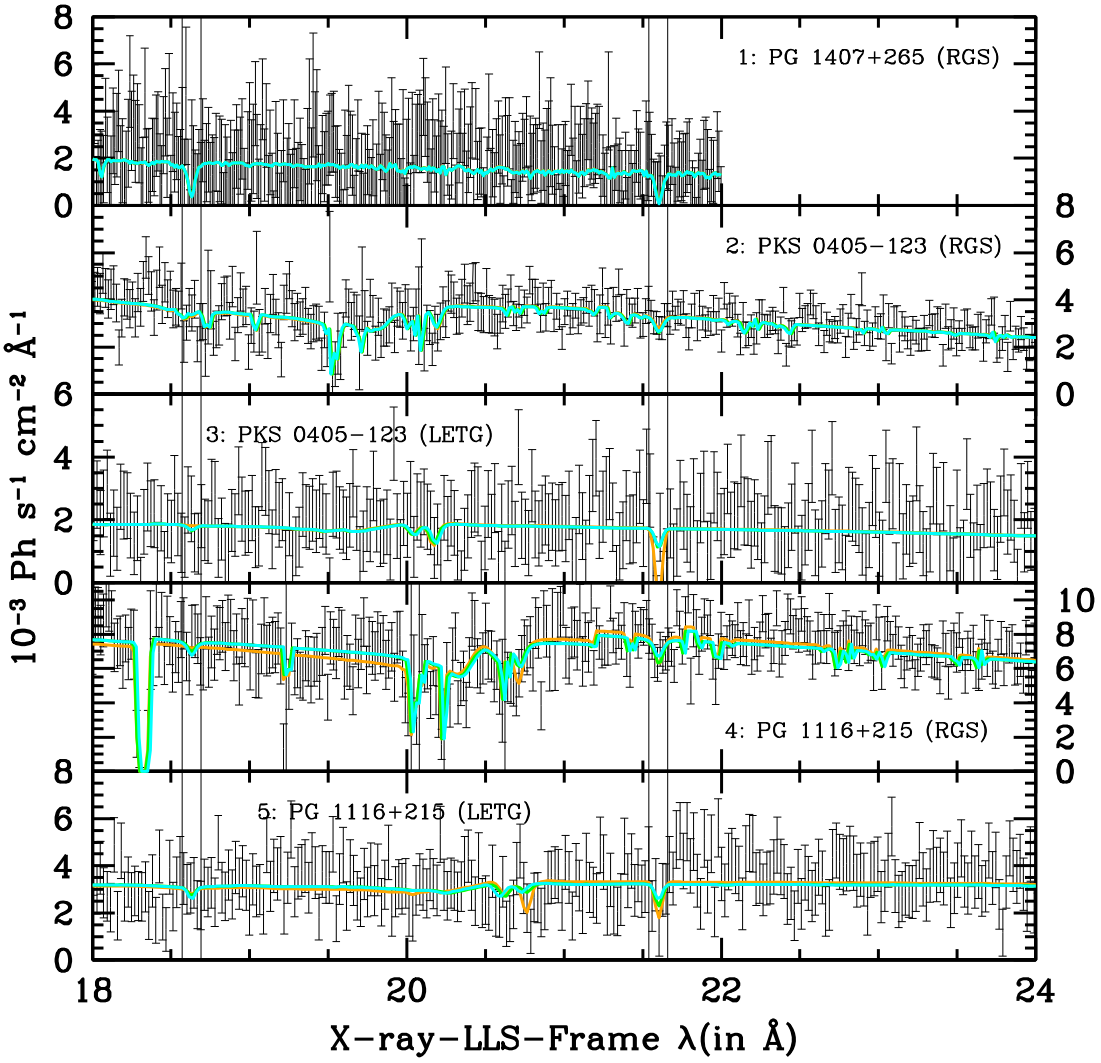

Figure 3. Raw Chandra LETG and XMM-Newton RGS data of the targets of the X-ray halo in each X-ray–LLS frame 18–24 Å wavelength range (vertical error bars). In each panel, the solid lines are the best-fitting continuum plus Gaussian absorption models for methods A (orange), B (green), and C (cyan), folded through their instrumental responses. The complex and prominent structures visible in the RGS spectra are instrumental features due to bad pixels in the dispersion detectors. The black rectangles mark the region containing the O VII Kα and Kβ transitions.

and FUV–LLS (right panels) frame continuum-normalized stacked spectra of the X-ray halo. To evaluate the centroid positions, EWs, and statistical significances of these lines, we performed standard spectral fitting of the stacked spectra. We did this by first exploiting the ftools (Blackburn 1995) "ftflx2xsp" and "ftgenrsp" to (a) convert the continuum-normalized stacked spectra of the X-ray halo into standard pulse-height analysis (PHA) formats and (b) build an over-simplified normalized photon redistribution matrix with a Gaussian LSF with an FWHM equal to the average RGS and LETG LSF FWHMs ($\Delta\lambda = 60$ mÅ). The continuum-normalized PHA spectra, folded with their responses, were then fitted in *Sherpa* with a model consisting of a constant plus two negative and unresolved (FWHM frozen to 10 mÅ) Gaussians, with all (continuum and line) parameters free to vary in the fit. The fits to both stacked spectra yielded values of the constant fully consistent with unity, and visual inspections showed flat residuals over the entire explored band, confirming the accuracy of the continuum modeling of the five RGS and LETG spectra described in Section 3.1. We then froze the constants to 1 and refit the data, obtaining the best-fitting line parameters and statistical significances (i.e., the ratio between the line EW and its 1σ statistical error) listed in Table 3, where we also list the 90% EW upper limit on the H-like oxygen Kα transition (forced in both spectra to have a frozen line centroid $\lambda_{\rm RF}^{\rm OVIIIK\alpha} = 18.63$ Å). The top part of the table is the result of the fit to the X-ray–LLS frame spectrum, while the bottom part lists the best-fitting parameters obtained on the FUV–LLS frame spectrum.

Figure 4 shows the data and best-fitting model (yellow curve) of both the X-ray–LLS (left panels) and FUV–LLS (right panels) stacked spectra of the X-ray halo. Contour plots of the EW centroid confidence levels of the two absorption lines are shown in Figure 5. Clearly, the O VII Kα and Kβ X-ray halo lines are present in both the stacked X-ray–LLS and FUV–LLS spectra. The relative position of the best-fitting Kα and Kβ line centroids in the FUV–LLS spectrum, $\Delta\lambda_{\rm K\alpha-Kbeta}^{\rm FUV-LLS}$, is offset from the rest-frame relative position of these transitions by ~ -1000 km s^{-1}, fully consistent with the observed distributions of the O VII Kα, Kβ (RGS) and O I, O II Kα (HRC-LETG) offsets in the Galactic samples of Nicastro et al. (2016b) and Nicastro et al. (2016a), respectively

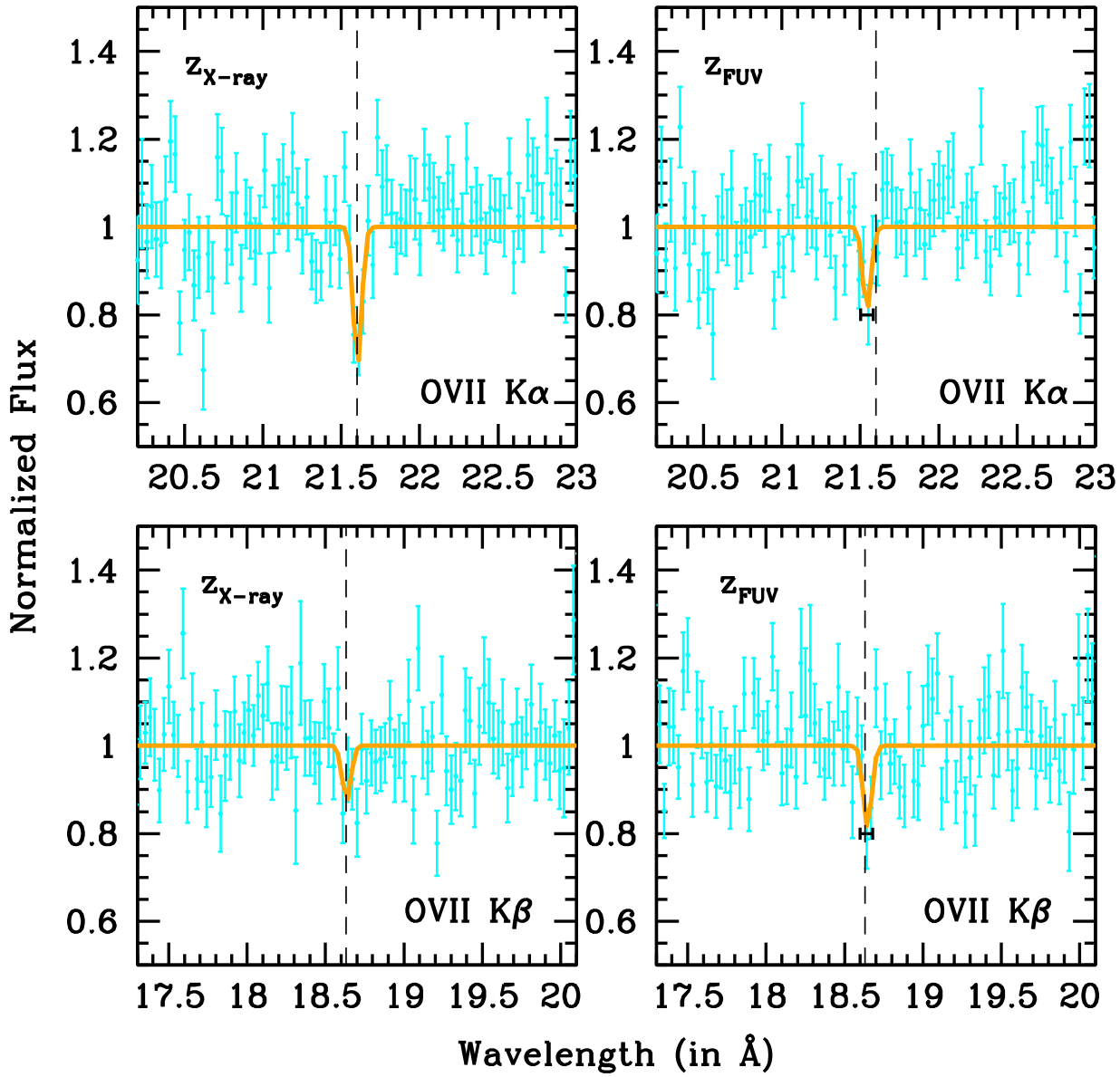

Figure 4. Two portions of the stacked X-ray–LLS (left panels) and FUV–LLS (right panels) frame spectra of the X-ray halo in continuum-normalized counts and wavelength ranges of 20.2–23 (top panels) and 17.3–20.1 (bottom panels) Å. The spectrum is binned at a resolution of 30 mÅ (about half the LSF FWHM of both instruments) and has SNRE = 29.3 in the continuum at $\lambda = 21.6$. The yellow curves are the best-fitting models. The fit yields combined (in quadrature) statistical significances of the O VII lines of 6.8σ (X-ray–LLS spectrum) and 4.7σ (FUV–LLS spectrum; Table 3).

(Figure 10). The line EWs measured in the two spectra are also consistent with each other within their 1σ–1.5σ statistical errors, as are the ratios of the O VII Kα/Kβ EWs and therefore the O VII column densities (see Section 4.1): $EW_{K\alpha}/EW_{K\beta} = 2.5 \pm 1.2$ and 1.0 ± 0.4 in the stacked X-ray–LLS and FUV–LLS, respectively.

The O VII Kα line is detected at the highest significance (6.4σ) and exactly $\lambda_{RF}^{OVIIK\alpha} = 21.6$ Å in the stacked X-ray–LLS spectrum. This is obviously by construction, as this spectrum is built by rigidly shifting, before stacking, each X-ray spectrum to its own X-ray–LLS redshift derived from the best-fitting position of the O VII Kα line in each spectrum and therefore should not be regarded as an accurate measurement of the actual probability of chance detection of the O VII Kα line in an X-ray halo (see also Sections 3.4 and 3.5). On the other hand, the statistical significance of the rigidly shifted O VII Kβ line is higher in the stacked FUV–LLS spectrum (i.e., at the exact FUV–LLS redshifts), as it is the 90% upper limit on the EW of the O VIII Kα transition at the LLS redshift (Table 3), probably confirming that RGS and LETG spectra suffer large uncertainties in their dispersion relationship, as demonstrated by the breadth of the distribution of Galactic-line relative-centroid offsets in Figure 10, and suggesting that a more reliable estimate of the O VII Kα and Kβ EW (and O VII Kα upper limit) lines from the X-ray halo lies somewhere in between the 4.7σ and 6.8σ derived from the stacked X-ray–LLS and FUV–LLS spectra, respectively, and probably closer to the lower boundary of this range.

3.4. Statistical Significance of the X-Ray Halo

The total (coadded in quadrature) statistical significance of the O VII lines of the X-ray halo that we derive from the fitting to the continuum-normalized stacked X-ray–LLS and FUV–

Table 3
Best-fitting X-Ray Halo Absorption Line Parameters

Line Parameter	O VII Kα	O VII Kβ	O VIII Kα
X-Ray–LLS Spectrum			
Centroid (in Å)	$21.604^{+0.007}_{-0.006}$	$18.64^{+0.08}_{-0.02}$	18.97[a]
EW (in mÅ)	21.6 ± 3.4	8.6 ± 4.0	$\leqslant 7.9$
Significance	6.4σ	2.2σ	90%
Combined significance		6.8σ	
FUV–LLS Spectrum			
Centroid (in Å)	$21.54^{+0.02}_{-0.01}$	$18.647^{+0.009}_{-0.010}$	18.97[a]
EW (in mÅ)	12.9 ± 3.9	12.9 ± 3.8	$\leqslant 11.4$
Significance	3.3σ	3.4σ	90%
Combined significance		4.7σ	

Note.
[a] Frozen in the fit.

LLS spectra is 6.8σ and 4.7σ, respectively. The first of these two should, in principle, be compared to the 5.6σ statistical significance obtained by simultaneously fitting the five X-ray spectra independently with method A (left panel of Figure 2), while the second should be compared to either the 4.6σ or 4.2σ obtained through joint-fitting methods B or C (middle and right panels of Figure 2), respectively.

In all cases, the difference in statistical significance between the joint- and stacked-fitting methods is probably explained by (a) the rigidity of the condition on the relative position of the O VII Kα and Kβ lines in each spectrum (frozen to the rest-frame relative position), which is instead relaxed in the fit to the stacked spectra, where the centroids of both the Kα and Kβ Gaussians are left free to vary in the fit (which yields a relative offset of the Kα–Kβ transitions of about +10 and 60 mÅ for the stacked X-ray–LLS and FUV–LLS spectra, respectively; see Table 3), and, (b) most importantly, the oversimplified Gaussian-shaped LSF assumed to build the average RGS+LETG response that we use to fit the stacked spectra (see Section 3.3). Indeed, while a Gaussian-shaped LSF is an excellent approximation of the HRC-LETG LSF, the RGS LSF is better approximated by a Lorentzian, with broad wings due to electron scattering of photons from the reflection gratings to the dispersive detectors. The actual statistical significance of the O VII signal from the X-ray halo thus lies somewhere between 5.6σ and 6.8σ (joint-fitting method A versus stacked X-ray–LLS fitting) or 4.2σ and 4.7σ (joint-fitting method C versus stacked FUV–LLS fitting), and it is probably best estimated by the 4.6σ–4.7σ significances derived through the joint-fitting method B or the fitting to the stacked FUV–LLS spectrum (one-sided chance-detection probabilities of $1.3–2 \times 10^{-6}$, increasing to $0.8–1.2 \times 10^{-5}$ after conservatively allowing for redshift trials; see Section 3.5).

3.5. Probability of Chance Detection/Identification of the X-Ray Halo

Strong intervening O VII Ka absorbers are rare. Recent hydrodynamical simulations predict that the Universe's random line of sight intercepts 0.17 O VII Ka absorbers per unit redshift with rest-frame EW $\geqslant$ 18 mÅ (250 km s^{-1} at 21.6 Å; e.g., Figure 6, left panel in Wijers et al. 2019). Such strong absorbers are practically all in halos (Figure 6, top right panel in Wijers et al. 2020), but only about half of these absorbers come from halos with masses between 10^{12} and $10^{12.5}$ $M_{\odot}$ (the range of masses of the galaxy halos associated with our three LLSs with galaxy association). The chance probabilities of expecting $0.17 \times z$ such absorbers and seeing one, up to the redshifts of our background quasars, are thus 0.015, 0.043, and 0.043 for PG 1116+215, PG 1407+265, and PKS 0405–123, respectively. Analogously, the probability of seeing none up to the redshift of PG 1216+069 (for which no galaxy association is reported), out of any mass halo, is 0.95. Finally, then, the chances of seeing one O VII Kα system with EW $\geqslant$ 250 km s^{-1} (rest-frame) along three out of the four lines of sight whose X-ray spectra are sensitive to such EWs at $>1.5\sigma$ is $P_{\rm theory}(3|4) = 0.015 \times 0.043 \times 0.043 \times 0.95 = 2.6 \times 10^{-5}$, which is to be excluded at $\geqslant 4.2\sigma$ confidence.

This is the chance-identification probability of seeing the system at any redshift in the allowed intervals. Here, instead, we use the FUV–LLS redshifts as priors, so the chance-identification probability should be further weighted by the chance-detection probability of the X-ray lines computed by accounting for a number of redshift trials around the expected FUV–LLS line position that allows for at least the observed X-ray–LLS and FUV–LLS redshift offsets. To be extremely conservative, we allow for three resolution elements ($>1.25\times$ the maximum observed offset in the HRC-LETG spectrum of PG 1116+215) and an oversampling of each resolution element by a factor of 4, i.e., a total of 12 trials per target spectrum. Fluctuations, however, could be either positive or negative in equal number. So, the number of redshift trials should be divided by 2 when assessing the significance of the absorption-only lines, that is, a total of six trials for each of the three targets, given our priors. Our three O VII Kα absorbers are seen at statistical significances of 1.7σ, 2.8σ, and 2.8σ in the X-ray spectra of our targets (Section 3.1), implying associated z-trial chance-detection probabilities of $P_{z\text{-trial}}(1.7\sigma) = [1 - P_{\rm Gauss}(1.7\sigma)] \times (12/2) = 0.53$, $P_{z\text{-trial}}(2.8\sigma) = 0.031$, and $P_{z\text{-trial}}(2.8\sigma) = 0.031$. The lines of sight are all independent, so the chance probability of seeing three O VII Kα lines out of three (the fourth target lacks the important prior of galaxy association) within the expected redshifts $\pm$ observed offset is the product of the three: $P_{z\text{-trial}}(3|3) = 0.53 \times 0.031 \times 0.031 = 0.00051$, to be excluded at $\geqslant 3.5\sigma$ (which would rise to $\geqslant 4.4\sigma$ if the Kβ lines were also considered).

Finally, then, the chance of detecting the three O VII Kα lines at their statistical significances and down to the observed EW (or column density), and that these are not associated with hot gas in the three galaxy association halos, is given by $P_{\rm theory}(3|4) \times P_{z\text{-trial}}(3|3) = 2.6 \times 10^{-5} \times 0.00051 = 1.3 \times 10^{-8}$, which can be excluded with a Gaussian-equivalent statistical significance of $\geqslant 5.6\sigma$. In such an unlikely event, the O VII Kα lines seen in the spectra of our three targets at redshifts consistent (or marginally consistent) with those of the LLSs and their galaxy associations, if real, would have to be imprinted by either diffuse warm–hot intergalactic medium gas or hot galaxy halos different from those associated with the LLSs, but in either case at redshifts very close to those of the three LLSs.

4. Discussion

The estimate of the line EWs from highly ionized oxygen in the spectrum of the X-ray halo, possibly at least partly associated with the moderately ionized oxygen seen at the LLS redshifts in the FUV spectra of the targets of our sample (Table 5; Fox et al. 2013), allows us to assess the physical state of the hot CGM in the X-ray halo.

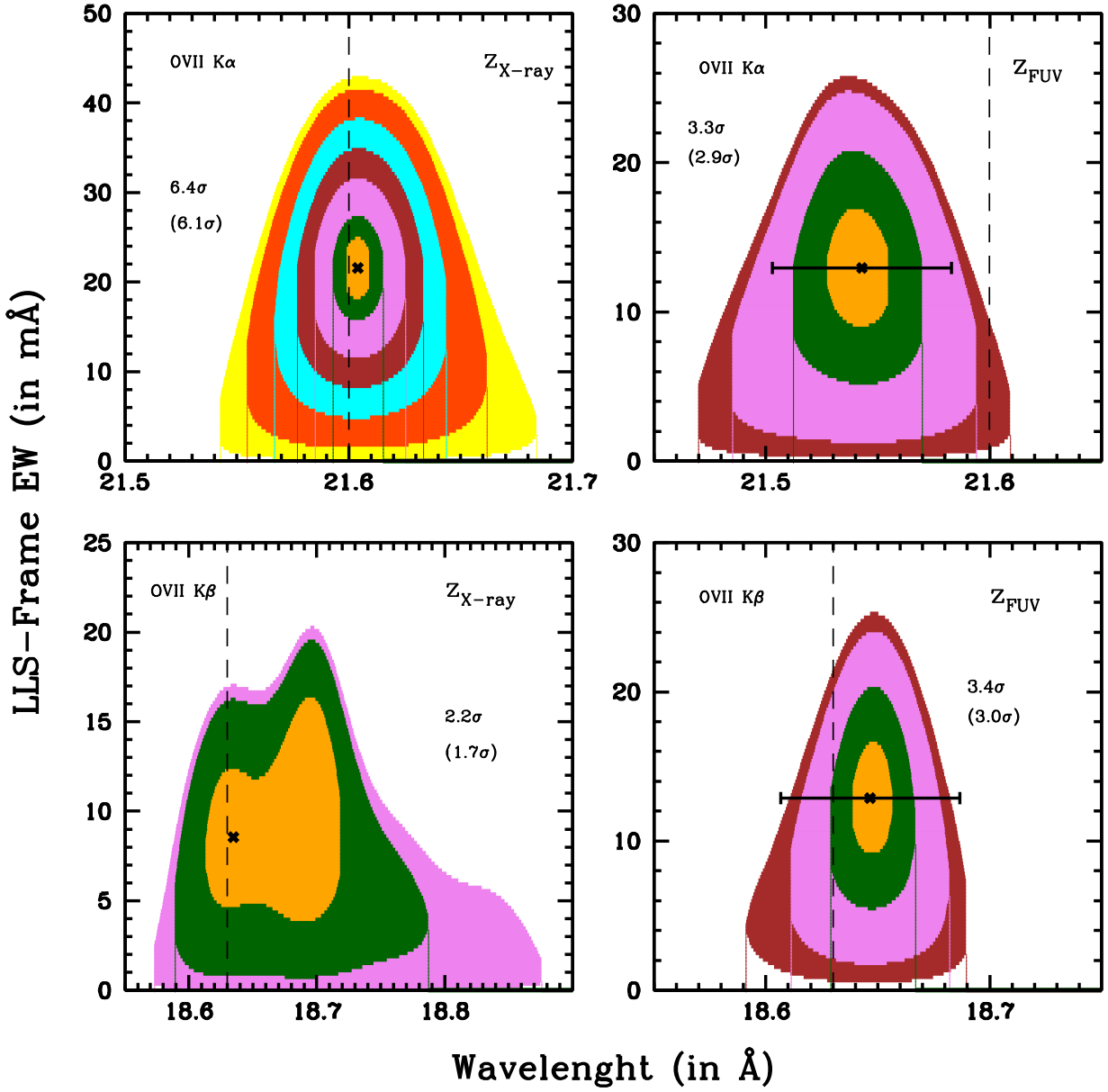

Figure 5. The O VII Kα (top panels) and Kβ (bottom panels) line EW-position confidence-level contours, up to the highest closed contour level, in the fits to the continuum-normalized stacked X-ray–LLS (left panels) and FUV–LLS (right panels) spectra of the X-ray halo. In each panel, the statistical significance of the highest closed contour is labeled for both one and two interesting parameters.

The O VII Kα and Kβ EW ratios in the stacked X-ray–LLS and FUV–LLS spectra are consistent with each other within their 1σ statistical uncertainties, and so are the implied O VII columns. These ratios amount to $EW_{K\alpha}/EW_{K\beta} = 2.5 \pm 1.2$ and 1.0 ± 0.4 in the stacked X-ray–LLS and FUV–LLS spectra, respectively, and are significantly smaller than the expected optically thin ratio (i.e., $EW_{K\alpha}/EW_{K\beta} = (f_{K\alpha}/f_{K\beta}) \times (\lambda_{K\alpha}/\lambda_{K\beta})^2 \simeq 6.4$, where f is the oscillator strength of the transition), suggesting a high degree of saturation of the lines and thus a relatively large column density and/or small Doppler parameter. In the following, we derive estimates of the O VII (and upper limits on the O VIII) column density through the X-ray halo by also exploiting the constraints on the weighted-average O VI Doppler parameter and column density.

4.1. Ion Column Densities and Doppler Parameter of the Hot CGM in the X-Ray Halo

The resolution of the current X-ray spectrometers is not sufficient to resolve the X-ray halo lines; thus, the estimate of the ion column densities N_{ion} and Doppler parameters $b_{ion} = \sqrt{2kT/m_{ion} + \sigma^2_{turb}}$ (where T is the electron temperature of the gas, m_{ion} is the ion mass, k is the Boltzmann constant, and σ^2_{turb} is the line-of-sight gas turbulence) must rely on the exploitation of curve-of-growth (CoG) techniques (e.g., Nicastro et al. 2002, 2005; Williams et al. 2005). We used our accurate Voigt profile routines (Nicastro et al. 1999) to produce a number of CoGs for each of our two O VII transitions and for ranges of values of $\log N_{O\,VII}(\text{in cm}^{-2}) = 12$–19 and

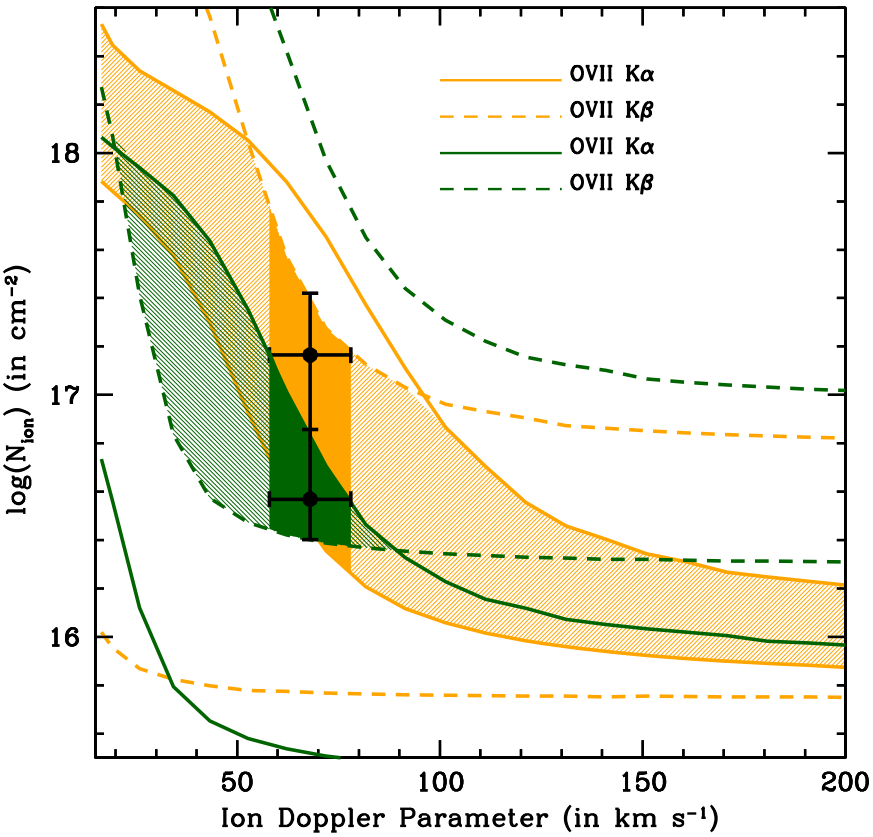

Figure 6. Solid and dashed curves show, respectively, the 90% $\log N_{\rm O\ VII} b$ contours as derived from the O VII Kα and Kβ transitions measured in the stacked X-ray–LLS (orange) and FUV–LLS (green) spectra of the X-ray halo. Light shaded orange and green regions show the 90% $\log N_{\rm O\ VII} b$ solutions for the two spectra, further reduced into the dark shaded orange and green regions by the fiducial weighted-average value $b_{\rm O} = 68 \pm 10$ km s^{-1} measured for O VI in the FUV spectra of our sample (black points with error bars). In this $b_{\rm O}$ interval and in both the X-ray–LLS and FUV–LLS spectra, the 90% low-boundary constraint on the Kα (X-ray–LLS spectrum; lower solid orange line) or Kβ (FUV–LLS spectrum; lower dashed green line) transition sets solid and similar floors to the column density of O VII through the X-ray halo at a distance of 115 kpc from the galaxy center.

$b^{\rm O} = 16$–200 km s^{-1} (the low boundary being set by imposing the minimum gas temperature of $T \geqslant 2.5 \times 10^5$ K needed to start producing sensible fractions, $\geqslant$0.1, of He-like oxygen in CIE gas; see Figure 11 in Appendix D), and unlikely absence of line-of-sight turbulence motion - $\sigma^2_{\rm turb} = 0$) and searched for the $N_{\rm O\ VII}$–$b_{\rm O}$ solutions that matched our EW measurements for both the X-ray–LLS and FUV–LLS stacked spectra. These are shown as orange and green light shaded regions, respectively, in Figure 6. We find the two broad (and similar) ion column density intervals $\log N_{\rm O\ VII}$(in cm^{-2}) $\simeq$ 15.9–18.5, $b_{\rm O} > 16$ km s^{-1} and $\log N_{\rm O\ VII}$(in cm^{-2}) $\simeq$ 16.4–18, $b_{\rm O} = 20$–88 km s^{-1} in the X-ray–LLS and FUV–LLS spectra, respectively.

The range of Doppler parameter values that we measure for oxygen is consistent with many of the LLS O VI Doppler parameters reported in the literature, in particular those of our three LLSs ($b^i_{\rm OVI} = 28$, 78, and 47 km s^{-1} for LLS 1, LLS 2, and LLS 3, respectively; Fox et al. 2013). If only due to thermal motion (i.e., $\sigma^2_{\rm turb} = 0$), $b_{\rm O\ VII} \sim 20$–88 km s^{-1} (as conservatively measured in the FUV–LLS spectrum) would correspond to temperatures in the interval $T \simeq (0.25$–$7.5) \times 10^6$ K. The exact value of b in this broad interval, however, is not critical with respect to the minimum ion column densities (and thus mass of the X-ray halo) allowed by the X-ray data. Figure 6 shows that in both the X-ray–LLS and FUV–LLS spectra, the 90% low-boundary constraint on the Kα (X-ray–LLS spectrum; lower solid orange line) or Kβ (FUV–LLS spectrum; lower dashed green line) transition sets stringent lower boundaries on the He-like oxygen column density through the X-ray halo at a distance of 115 kpc from the galaxy center. These are virtually independent on the Doppler parameter in the ranges $b_{\rm O\ VII} \gtrsim 50$ and 100 km s^{-1} (depending on whether the X-ray–LLS or FUV–LLS solutions are considered; optically thin limit), whereas $16 \lesssim b_{\rm O\ VII} \lesssim 50$ and 100 km s^{-1} (optically thick regimes) would imply even higher O VII column densities. In the following, we assume that the LLS-associated O VI absorbers seen in the FUV spectra of our targets are imprinted at least partly by the X-ray halo. Part of the FUV-detected O VI could belong to a different phase (e.g., Ahoranta et al. 2021), but, given the nondetection of O VIII in the X-ray data (up to the 90% upper limits listed in Table 3), it is reasonable to assume that at least part of it is produced by the O VII-bearing phase (see Section 4.2 and Appendix D). Accordingly, we consider the measured weighted-average O VI column (plus its 90% error) as an upper limit for the O VI column through the X-ray halo (see Section 4.2) and estimate O VII column densities at $\langle b_{\rm O\ VI} \rangle = 68 \pm 10$ km s^{-1}, the $(\sigma^i_{\rm OVII} \times N^i_{\rm OVI})$-weighted average of the three O VI absorbers. This corresponds to the X-ray halo virial temperature $\log T$(in K) $\simeq 6$ (see below) for internal line-of-sight turbulence $\sigma^2_{\rm turb} \simeq 48$–$71$ km s^{-1}.

In the following, we assume the two dark shaded orange and green regions of Figure 6 as the ranges of O VII column densities

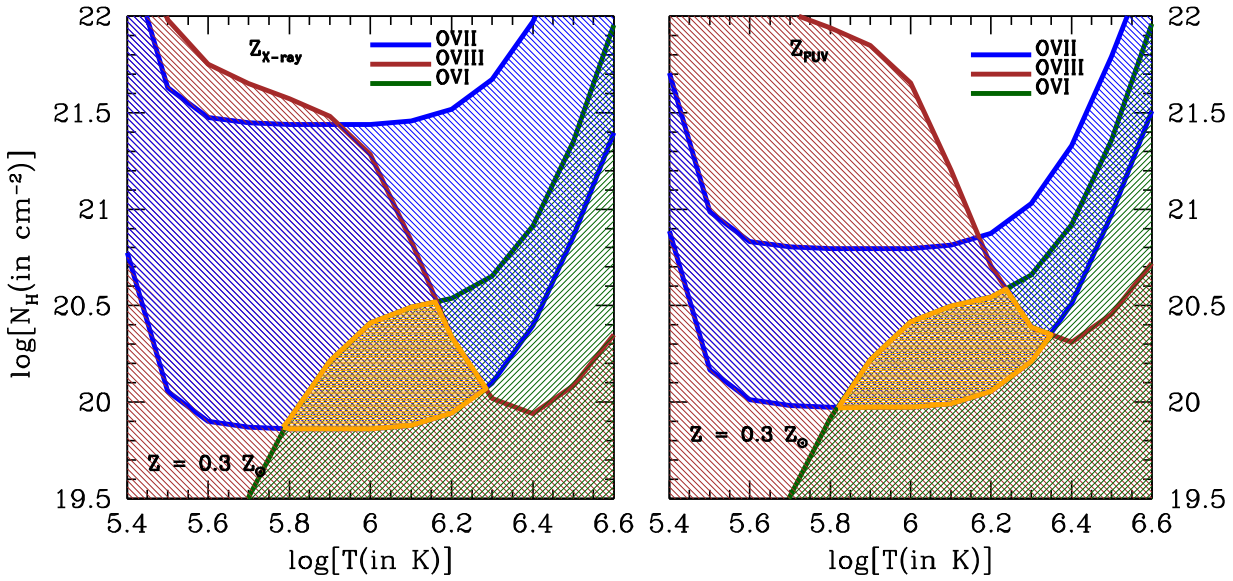

Figure 7. Constraints on the equivalent hydrogen column density of the X-ray halo at a projected distance $\langle\rho\rangle = 115$ kpc, obtained by dividing the ion column densities of O VII (blue curves and shaded area), O VIII (brown curve and shaded area), and average O VI (green curve and shaded area; Fox et al. 2013) at the weighted-average $\langle b_{\rm O\,VI}\rangle = 68 \pm 10$ km s^{-1} by their ion fractions in CIE gas (see Appendix D) and by the average $Z = 0.3\ Z_{\odot}$ metallicity observed for our three cool CGM systems as a function of the temperature of the hot CGM gas. The H-like ion of oxygen is not detected in the X-ray halo spectrum, and its column density curve in the figure is a 90% confidence upper limit (brown curve and shaded region). Instead, O VI is detected in the FUV spectra but considered here as an upper limit to allow for at least a portion of this ion to be produced in physical phases different from the O VII-bearing phase. The left panel is for the stacked X-ray–LLS spectrum, while the right panel shows solutions for the FUV–LLS spectrum.

allowed, respectively, by the X-ray–LLS and FUV–LLS spectra: $N_{\rm OVII}^{\rm X-ray-LLS} \simeq (1.9\text{–}60) \times 10^{16}$ and $N_{\rm OVII}^{\rm FUV-LLS} \simeq (2.4\text{–}16) \times 10^{16}$ cm^{-2}. We also consider the 90% upper limits on the EW of the O VIII Kα transition, inferred by the data at $\langle b_{\rm O\,VI}\rangle = 68$ km s^{-1} (Table 3), which yield 90% O VIII columns $N_{\rm OVIII}^{\rm X-ray-LLS} \leqslant 10^{16}$ and $N_{\rm OVIII}^{\rm FUV-LLS} \leqslant 2.3 \times 10^{16}$ cm^{-2} in the X-ray–LLS and FUV–LLS spectra, respectively.

4.2. Temperature and Equivalent Hydrogen Column Density

The virial temperature of a $z = 0.276$ halo with $\langle M_h\rangle = 10^{12.1}\ M_{\odot}$ and $\langle R_{\rm vir}\rangle = 195$ kpc (Table 5) is $\langle T_{\rm vir}\rangle = \frac{\mu_p G \langle M_h\rangle m_p}{2k\langle R_{\rm vir}\rangle} \simeq 10^6$ K (Qu & Bregman 2018), where $\mu_p = 0.59$ is the average weight per particle for a fully ionized gas. At this temperature, He-like oxygen largely dominates the ionic abundance distribution of oxygen in CIE gas (left panel of Figure 11 in Appendix D), with the H- and Li-like ions being only $\simeq$2% and $<$1% of the total, respectively. The Li-like oxygen can be more efficiently produced in either CIE gas with $T \lesssim 4 \times 10^5$ K (close to the lowest considered value, $T = 2.5 \times 10^5$ K, for the O VII-bearing hot CGM) or low-density ($n_b < 10^{-4}$ cm^{-3}) gas photoionized by the external metagalactic radiation field (left and right panels of Figure 11 in Appendix D). Thus, the observed O VI could at least partly belong to CGM phases that are different from the O VII-bearing hot CGM phase, including the possibly photoionized cool CGM. We therefore conservatively infer the temperature and equivalent hydrogen column density of the hot gas permeating the X-ray halo at an average projected distance of 115 kpc from the galaxy center (about 0.6$\times$ the virial radius of our X-ray halo) by combining all of the available FUV and X-ray ion column density constraints but treating the measured average X-ray halo O VI column density (plus its 90% uncertainty) as an upper limit (shaded green regions of Figure 7).

Practically, we compute ion-by-ion equivalent hydrogen column densities $N_{\rm H}$ as follows. We first devide the $N_{\rm O\,VI}$, $N_{\rm O\,VII}$, and $N_{\rm O\,VIII}$ ion column densities by (1) the $\sigma^i_{\rm OVII}$-weighted average metallicity $\langle Z\rangle \simeq 0.3\ Z_{\odot}$ reported for the three cool LLS absorbers of our sample (which we use in a parametric form in the following to explicitly allow for possible hot and cool CGM differences, Wotta et al. 2019; Table 5), and (2) by the temperature-dependent $f_{\rm O\,VI}$, $f_{\rm O\,VII}$, $f_{\rm O\,VIII}$, and $f_{\rm NVI}$ ion fractions in CIE gas (see details and caveats in Appendix D) in the temperature range $\log T = 5.4\text{–}6.6$. This procedure yields ion-dependent $\log N_{\rm H}$–T solutions, whose intersection defines the common $\log N_{\rm H}$–T solution (shaded orange regions in the two panels of Figure 7). These span similar ranges in the X-ray–LLS and FUV–LLS spectra. In particular, for the X-ray–LLS spectrum (left panel), we find allowed intervals of $\log T^{\rm X-ray-LLS}$(in K) $= 5.77\text{–}6.27$ and $\log N_{\rm H}^{\rm X-ray-LLS}$(in cm^{-2}) $= (19.86\text{–}20.51) - \log(Z/0.3\ Z_{\odot})$, while the FUV–LLS spectrum (right panel) allows for slightly higher temperatures of $\log T^{\rm FUV-LLS}$(in K) $= 5.82\text{–}6.35$ and equivalent hydrogen column densities of $\log N_{\rm H}^{\rm FUV-LLS}$ (in cm^{-2}) $= (19.96\text{–}20.59) - \log(Z/0.3\ Z_{\odot})$. In both cases, the allowed temperature intervals encompass the $\langle T_{\rm vir}\rangle \simeq 10^6$ K virial temperature of the X-ray halo and are set by the intersections of the X-ray constraints on the O VII column density with the FUV $N_{\rm O\,VI}$ measurements (considered here as upper limits; green solid curve of Figure 7) and the X-ray $N_{\rm O\,VIII}$ upper limit (brown solid curve of Figure 7) on the lower and upper sides, respectively. More importantly, in both the X-ray–LLS and FUV–LLS spectra, the minimum equivalent hydrogen column density (and thus the amount of hot gas in the X-ray halo) is uniquely set by the very similar X-ray constraints on the lowest possible column density of O VII, while its upper boundaries are set again by the FUV $N_{\rm O\,VI}$ and X-ray $N_{\rm O\,VIII}$ upper limits.

Indeed, O VI alone would favor solutions at temperatures of $\log T$(in K) $\simeq 5.4\text{–}5.6$ (where the O VI ion fraction is $\gtrsim$0.1 in CIE gas; see Figure 11 in Appendix D), which would yield

equivalent hydrogen column densities (and thus baryonic masses) at least an order of magnitude lower than the boundaries set by the O VII X-ray measurements in the two stacked spectra of the X-ray halo. If only X-ray oxygen data are considered instead, the low boundary of the temperature interval is uniquely set by the need to produce detectable fractions of O VII (i.e., log$T$(in K) $\gtrsim$ 5.4), but the equivalent hydrogen column density (and thus the baryonic mass; see below) is still lower-bounded at $\log N_{\rm H}^{\rm X-ray-LLS}$(in cm^{-2}) $\simeq$ 19.86 − log (Z/0.3 $Z_{\odot}$) or $\log N_{\rm H}^{\rm FUV-LLS}$(in cm^{-2}) $\simeq$ 19.96 − log (Z/0.3 $Z_{\odot}$) and allowed to be as large as $\log N_{\rm H}^{\rm FUV-LLS}$(in cm^{-2}) $\simeq$ 20.85 − log (Z/0.3 $Z_{\odot}$) or as implausibly large as $\log N_{\rm H}^{\rm X-ray-LLS}$(in cm^{-2}) $\simeq$ 21.45 − log (Z/0.3 $Z_{\odot}$). It is only by combining the FUV and X-ray column density constraints that we can set stringent lower and upper limits to both the temperature and the equivalent hydrogen column density (and, in turn, mass; see below) of the X-ray halo.

4.3. Mass of the Hot CGM in the X-Ray Halo

Despite the very similar ranges of temperature and equivalent hydrogen column density allowed by either the stacked X-ray–LLS or FUV–LLS spectra, in the following, we continue providing separate estimates for the two cases for both the line-of-sight volume density of the hot CGM and its mass.

Our idealized model for the X-ray halo is that of a sphere centered at the galaxy center and filled with two gaseous phases (cool and hot, each isothermal) mutually complementing each other spatially. The hot phase is diffuse and extends from the galaxy center out to the virial radius $R_{\rm vir}$, with density decreasing radially. The cool and condensed phase is that of our three LLSs, observed in the FUV through low-ionization metals and H (e.g., Lehner et al. 2013).

To estimate the average density of the hot CGM phase of the X-ray halo, we need to estimate the maximum line-of-sight path length available for the hot gas, which, under our assumptions, is simply given by the total available path length covered by the X-ray halo at the projected distance of $\langle\rho\rangle$ minus the thickness of the cool CGM clouds along the line of sight. With the assumed geometry, the path length crossed by our lines of sight at a projected distance $\langle\rho\rangle$ and through the X-ray halo is simply given by $L = 2\sqrt{\langle R_{\rm vir}\rangle^2 - \langle\rho\rangle^2} \simeq 315$ kpc. The ratio between the total thickness of the cool CGM clouds along the line of sight (i.e., the diameter of a single spherical cloud times the number of clouds shadowing each other along the line of sight; i.e., Stocke et al. 2013) and L defines the line-of-sight covering factor of the cool phase $f_l^{\rm cool}$. The total thickness of the cool CGM clouds has been estimated for several LLSs by matching the measured ion column densities with predictions by photoionization equilibrium models in which a halo cloud of gas with constant density $n_{\rm H}^{\rm cool}$ is illuminated by the metagalactic radiation field at the redshift of the LLS (e.g., Lehner et al. 2013; Stocke et al. 2013). For our three LLSs, Lehner et al. (2013) and Stocke et al. (2013) derived $N_{\rm H} = (10^{20}, 10^{18.55}, 10^{19.1})$ cm^{-2} and $n_{\rm H} = (10^{-3.1}, 10^{-3.1}, 10^{-4})$ cm^{-3} for (LLS 1, LLS 2, LLS 3), respectively. This gives $\sigma^i_{\rm OVII}$-weighted averages of $\langle N_{\rm H}\rangle^{\rm cool} = 10^{19.469}$ cm^{-2} and $\langle n_{\rm H}^{\rm cool}\rangle = 5.2 \times 10^{-4}$ cm^{-3} for the cool CGM of the X-ray halo and thus a line-of-sight thickness of the clouds of l(X-ray − halo) $\simeq$ 18 kpc. This yields a line-of-sight covering factor of the cool CGM through the X-ray halo of $f_l^{\rm cool} = 0.057$.

Finally, the average density of the hot CGM phase at a projected distance $\langle\rho\rangle = 115$ kpc through the X-ray halo is thus given by $\langle n_{\rm H}^{\rm hot}\rangle = N_{\rm H}^{\rm hot}/[(1 - f_l^{\rm cool})L] \simeq$ (8–35) $\times 10^{-5}(Z/0.3Z_{\odot})^{-1}$ cm^{-3} (X-ray–LLS spectrum) or $\langle n_{\rm H}^{\rm hot}\rangle = \simeq$(10–42) $\times 10^{-5}(Z/0.3Z_{\odot})^{-1}$ cm^{-3} (FUV–LLS spectrum), and it modulates by a factor of $n_{\rm H}^{\rm hot}(@\rho;\, l = 0)/n_{\rm H}^{\rm hot}(@\rho;\, l = \pm L/2) \simeq [1 + (L/2\rho)^2]^{3\beta/2} \simeq 3^{3\beta/2}$ from the near side through the far side of the halo (here $@\rho; l =$ means the equivalent H density at the impact parameter distance ρ from the center of the galaxy and at line-of-sight length l, and β is the spectral index of the density profile we adopt to estimate the mass of the hot CGM; see below). The average density is thus only $\lesssim 7(Z/0.3Z_{\odot})^{-1}\times$ lower than that estimated for the cool CGM phase under the pure photoionization equilibrium and constant gas density hypothesis. This combined with temperatures of the two phases that differ by a factor of ∼100 gives pressures that differ by factors $\gtrsim$14(Z/0.3 $Z_{\odot}$). Pressure equilibrium between the two phases would then require either $\gtrsim$14(Z/0.3 $Z_{\odot}$)× lower temperatures of the hot phase, inconsistent with the reported detection of O VII, or $\gtrsim$14(Z/0.3 $Z_{\odot}$)× lower average densities of the hot phase along the line of sight, which, in turn, would require unphysically long line-of-sight path lengths of $\gtrsim$4(Z/0.3 $Z_{\odot}$) Mpc. This suggests that either pressure equilibrium between the two coexisting phases is not at work or the cool CGM clouds are actually $\gtrsim$14(Z/0.3 $Z_{\odot}$)× denser (and thus smaller) than inferred under the pure photoionization hypothesis. In the latter case, the average linear size of the cool CGM clouds would be of the order of 1–2 kpc, i.e., similar to that inferred by the angular size of typical Galactic H I compact high-velocity clouds (CHVCs) if at a distance of ∼100 kpc from the Galaxy's center (e.g., Putman et al. 2012). At such cool CGM densities, photoionization by the external radiation field would be less effective, and alternative (or concurring) ionization mechanisms should be at work (see, e.g., Bregman et al. 2018, and references therein), but the cool CGM clouds could then be pressure-confined by the hot gas (e.g., Armillotta et al. 2017; Afruni et al. 2021, and references therein).

To estimate the mass of the hot phase, we assume a volume filling factor $(1 - f_V^{\rm cool}) = (1\text{–}0.75 \times f_l^{\rm cool}) \simeq 0.957$, again complementary to that estimated for the cool CGM (the factor of 0.75 accounts for the occurrence of LLS detections in the samples observed with the HST-COS, e.g., Werk et al. 2014, and references therein). For the radial baryon density law of the X-ray halo, we assume a β-profile (Cavaliere & Fusco-Femiano 1976), $n_{\rm H}^{\rm hot}(r) = n_0^{\rm hot}[1 + (r/R_c)^2]^{-3\beta/2}$. We integrate the density profile from $r = 0$ up to $r = R_{\rm vir}$ for a number of values of the model parameters, searching for those solutions that match the entire range of allowed hot CGM $N_{\rm H}$ observed at the average projected distance of $\langle\rho\rangle = 115$ kpc, i.e.,

$$N_{\rm H} = 2\int_0^{L/2} n_{\rm H}^{\rm hot}(r)dl = 2\int_0^{\alpha_{\rm max}} n_{\rm H}^{\rm hot}(\alpha;\, \rho)(\rho/\cos^2\alpha)d\alpha, \quad (1)$$

where dl is the increment along the line of sight, α is the angle between the projected distance ρ (i.e., the plane of the sky) and the radius of the halo at a line-of-sight depth of $l = \sqrt{r^2 - \rho^2} = \rho\ tg(\alpha)$, and $tg(\alpha_{\rm max}) = 2\sqrt{(R_{\rm vir}/\rho)^2 - 1}$.

Our X-ray halo has a dynamical mass of $\langle M_h\rangle \simeq 10^{12.1}\ M_{\odot}$, stellar mass of $\langle M^*\rangle \simeq 10^{10.53}\ M_{\odot}$, and, under the pure photoionization equilibrium hypothesis (i.e., assuming an average cloud gas density $\langle n_{\rm H}\rangle^{\rm cool} = 5.2 \times 10^{-4}$ cm^{-3}), cool CGM gas mass (within one virial radius) of $\langle M_{\rm cool\ CGM}\rangle \simeq 10^{10.27}\ M_{\odot}$ (Table 5). This yields a missing-

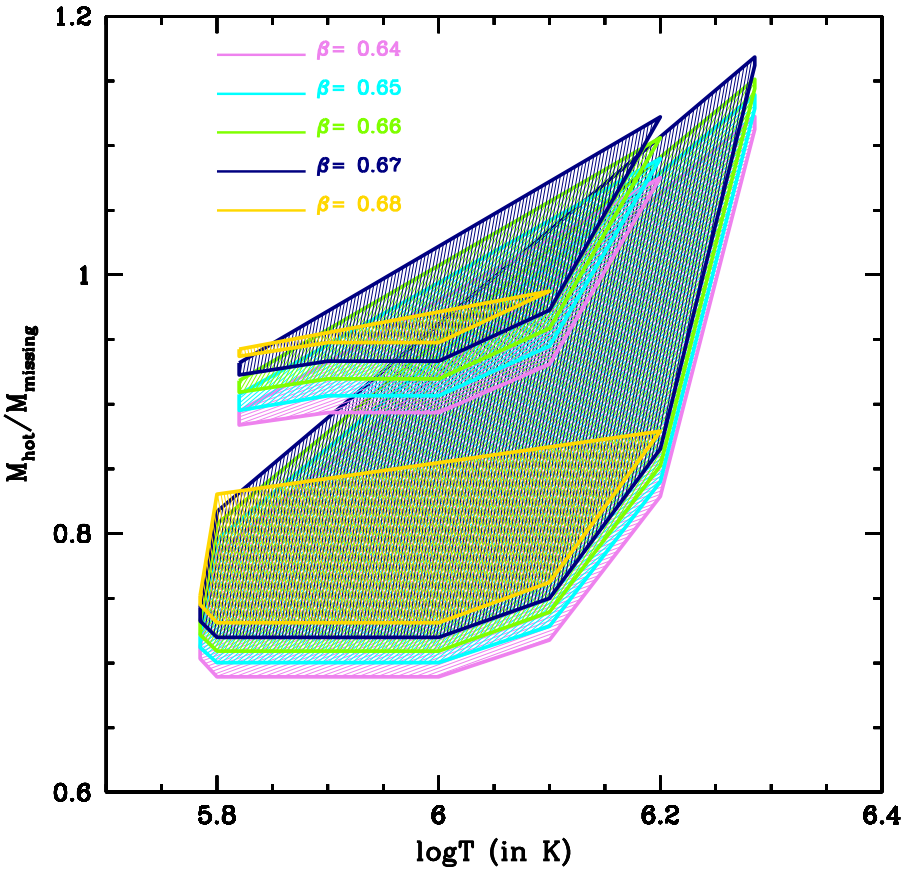

Figure 8. Constraints on the mass and temperature of the hot CGM in the X-ray halo as estimated from the X-ray–LLS (larger polygonal regions) and FUV–LLS (smaller polygonal regions) spectra for density spectral indices in the range $\beta = 0.64$–0.68 (isothermal halo) and hot CGM metallicity $Z = 0.3\ Z_{\odot}$.

baryon mass of $M_{\rm missing} = f_b \langle M_h \rangle - \langle M^* \rangle - \langle M_{\rm cool\ \ CGM} \rangle \simeq 1.45 \times 10^{11}\ M_{\odot}$ (where $f_b = 0.157$ is the universal baryon fraction; Planck Collaboration et al. 2020). By exploring reasonable values of the β-profile parameters, i.e., $n_0^{\rm hot} = 4 \times 10^{-4}$–$0.1\ {\rm cm}^{-3}$, $R_c = 1$–5 kpc (for reference, the central volume density and core radius of the hot halo of the Milky Way have been estimated in the ranges $n_0^{\rm MW} \simeq (0.12$–$1.2) \times 10^{-2}\ {\rm cm}^{-3}$ and $R_c = 1$–3, Bregman et al. 2018, or $n_0^{\rm MW} \simeq (0.7$–$6.6) \times 10^{-2}\ {\rm cm}^{-3}$ and $R_c = 0.6$–2.7, Nicastro et al. 2016b) and $\beta = 0.64$–0.68 (i.e., centered on the two-thirds value corresponding to an isothermal halo). Accepting only solutions at radii $r/R_{\rm vir} = 1.000 \pm 0.005$, we find ranges of allowed masses of $M_{\rm hot-CGM} \simeq (1$–$1.7) \times 10^{11} (Z/0.3Z_{\odot})^{-1}$ corresponding to temperatures in the interval $\log T({\rm in\ K}) \simeq 5.78$–$6.28$ for core radii and volume densities in the ranges $R_c = 3.5$–5 kpc and $n_c^{\rm hot} = 0.02$–$0.05\ {\rm cm}^{-3}$.

This mass is at least twice the combined mass of the stellar disk and cool CGM of the X-ray halo and, more importantly, at least 70% of the galaxy's missing mass $M_{\rm missing}$. The fraction of hot over missing baryons at the halo virial radius lies in the range $\xi_b = \frac{M_{\rm hot-CGM}}{M_{\rm missing}} \simeq (0.7$–$1.2)(Z/0.3Z_{\odot})^{-1}$, depending on the exact value of the density profile spectral index β (Figure 8, where smaller regions are estimates from the FUV–LLS spectrum, and larger regions are from the X-ray–LLS spectrum), with steeper profiles associated with higher central density, and thus mass, solutions. At the halo virial temperature, the fraction of hot over missing baryons of an isothermal halo ($\beta = 2/3$) lies in the range $\xi_b \simeq (0.72$–$1.02)(Z/0.3Z_{\odot})^{-1}$.

This not only implies that virtually all of the baryons that were still missing can now be accounted for by the hot CGM gas but also has important consequences for our understanding of the galaxy–CGM and galaxy–IGM feedback processes throughout the Universe's lifetime and can help refine feedback prescriptions in hydrodynamical simulations. A dense hot virialized CGM containing the vast majority of the expected baryons within its virial radius suggests that accretion mostly occurred in hot mode and at the rate given by the cosmological baryon fraction (e.g., van de Voort & Schaye 2012), while the feedback from supernovae and/or past nuclear activity was not sufficiently efficient to expel a significant fraction of the baryons beyond $R_{\rm vir}$. However, the relative metal richness of the cool, and thus probably the hot, CGM (Table 5) may point to an important contribution of feedback (e.g., supernova winds and/or past nuclear activity) for its metal pollution. In this scenario, we can speculate that the accretion of fresh gas to feed the star formation in the disk likely takes place via a slow cooling of the hot CGM (e.g., Fraternali 2017; Hafen et al. 2022).

Our simple spherical isothermal halo filled with a two-phase (cool and hot) gas is clearly an idealization. However, the low-boundary mass of the hot component ($M_{\rm hot\ \ CGM} \sim (1$–$1.3) \times 10^{11}\ M_{\odot}$, depending on whether the stacked X-ray–LLS or FUV–LLS spectrum is considered; Figure 8) is a rather strict and conservative limit imposed solely by the large amount of O VII seen in the stacked X-ray spectrum at a projected distance of $\sim 0.6\ R_{\rm vir}$. Flattening the density profile to $\beta = 0.4$ lowers the minimum fraction of missing mass allowed by the solutions by about 15% but increases the maximum allowed fraction by a

factor of ∼3 and can easily accommodate missing-baryon masses well within $R_{\rm vir}$. Reducing the volume covering factor of the hot component, increasing the hot CGM metallicity to >0.3 $Z_{\odot}$, modifying the geometry of the halo, and/or considering nonequilibrium, multitemperature collisional–ionization models (e.g., Gnat & Sternberg 2007) can help reduce the mass of the O VII-bearing gas but will still leave large portions of the density profile parameter space for solutions that close the galaxy baryon census.

5. Conclusions

We reported the first direct detection of O VII (Kα and Kβ) absorption in the stacked (or jointly fitted) X-ray spectra of three LLSs+O VI absorbers seen in the FUV and associated with the halos of three $\sim L^*$ galaxies. We identify the X-ray absorbers with large amounts of hot gas coexisting with the cool CGM of these systems and filling their halos. In summary, we found the following.

1. The X-ray halo is detected in the X-ray spectra of the three quasars PG 1417+265, PKS 0405−123, and PG 1116+215 via O VII Kα and Kβ lines at positions offset by the expected FUV–LLS frame positions by ∼300–1600 km s^{-1}, an offset velocity interval consistent with the centroid offset distributions observed in two samples of Galactic O VII Kα, Kβ and O I, O II Kα absorption lines.
2. The combined (Kα+Kβ) statistical significance of the X-ray halo is between 4.2σ and 5.6σ in the jointly fitted spectra of our five targets (and 4.7σ and 6.8σ in the stacked spectra of the X-ray halo).
3. The properties of the X-ray halo are those of the halo of a $\sim L^*$ galaxy with stellar mass $M_* = 10^{10.53}\ M_{\odot}$, virial radius $R_{\rm vir} \simeq 195$ kpc, virial temperature $T_{\rm vir} \simeq 10^6$ K, and halo mass $M_h = 10^{12.1}\ M_{\odot}$.
4. We estimate the mass of the cool CGM phase of the X-ray halo to be about half the average stellar mass of the three galaxies that host it, i.e., $M_{\rm cool\ CGM} = 10^{10.27}\ M_{\odot}$, which leaves a missing-baryon mass in the system of $M_{\rm missing} \simeq 1.45 \times 10^{11}\ M_{\odot}$.
5. Our line of sight intercepts the X-ray halo at a weighted-average projected distance of $\rho = 115$ kpc, i.e., ≃0.6 $R_{\rm vir}$, and, in a spherical configuration, has a path length of $L = 315$ kpc through the halo, along which we estimate equivalent hydrogen column densities of the O VII-bearing gas at the average $\langle b_{\rm O\ VI}\rangle = 68 \pm 10$ km s^{-1}, which are virtually independent on whether they are estimated from the best-fitting O VII (and upper limit on O VIII) EWs derived from the stacked X-ray–LLS or FUV–LLS spectra, i.e., $\log N_{\rm H}^{\rm X-ray-LLS}$(in cm^{-2}) = (19.86–20.51) − log(Z/0.3 $Z_{\odot}$) or $\log N_{\rm H}^{\rm FUV-LLS}$(in cm^{-2}) = (20.02–20.59) − log(Z/0.3$Z_{\rm sun}$) = (20.0220.59)$(Z/0.3Z_{\odot})^{-1}$.
6. By assuming a spherical geometry and a β-density profile for the X-ray halo, we derive hot CGM masses again largely independent on the stacking methodology and in the ranges $M_{\rm hot-CGM}^{\rm X-ray-LLS} = (1\text{–}1.7) \times 10^{11}(Z/0.3Z_{\odot})^{-1}$ and $M_{\rm hot-CGM}^{\rm FUV-LLS} = (1.3\text{–}1.6) \times 10^{11}(Z/0.3Z_{\odot})^{-1}\ M_{\odot}$, corresponding to missing-baryon fractions $\xi_b^{\rm X-ray-LLS} = \frac{M_{\rm hot-CGM}}{M_{\rm missing}} = (0.7-1.2)(Z\ /\ 0.3Z_{\odot})^{-1}$ and $\xi_b^{\rm FUV-LLS} = (0.92-1.02)(Z/0.3Z_{\odot})^{-1}$, and temperatures in the intervals $\log T$(in K)$^{\rm X-ray-LLS} \simeq$ 5.78–6.28, $\log T$(in K)$^{\rm FUV-LLS} \simeq$ 5.82–6.2, both comprising the X-ray halo virial temperature $T_{\rm vir} \simeq 10^6$ K.

Our findings imply that virtually all of the baryons that were still missing in typical L^* galaxies can now be accounted for by the hot CGM gas. This has important consequences for our understanding of the galaxy–CGM and galaxy–IGM feedback processes throughout the Universe's lifetime, suggesting that accretion in these galaxies mostly occurred in hot mode and at the rate given by the cosmological baryon fraction. Feedback from internal activity was efficient in metal polluting the CGM and perhaps hampering its cooling but not sufficient to expel a significant fraction of the baryons beyond $R_{\rm vir}$.

6. Scripts and Code Availability

This paper makes use of publicly available codes for spectral fitting (i.e., *Sherpa*) and custom-made Fortran90 and SuperMongo routines for (a) the CoG analysis (Fortran90; first developed, used, and published in Nicastro et al. 1999 and then also used in, e.g., Nicastro et al. 2005; Williams et al. 2005; Nicastro et al. 2018), (b) the X-ray halo mass calculation via β-profile functions (Fortran90), (c) the de-redshifting and regridding over a common spectral grid of individual source and background spectra and best-fitting continuum models (Fortran90), and (d) generating figures (SuperMongo). All custom-made routines and software shall be made available by the corresponding author upon request.

Acknowledgments

We thank the anonymous referees for the useful comments and suggestions, which helped to significantly improve the paper. F.N., S.B., M.B, A.B., A.D.R., C.F., E.P., and L.Z. acknowledge support from INAF-PRIN grant "A Systematic Study of the largest reservoir of baryons and metals in the Universe: the circumgalactic medium of galaxies" (No. 1.05.01.85.10). F.N., E.P., and L.Z. also acknowledge support from the EU grant AHEAD-2020 (GA No. 871158). T.F. acknowledges support by the National Key R&D Program of China No. 2017YFA0402600, NSFC grant Nos. 11890692 and 12133008, and the science research grants from the China Manned Space Project with No. CMS-CSST-2021-A04.

Facilities: XMM-Newton (RGS), Chandra (LETG), HST (COS).

Appendix A
Selection of the X-Ray Halo Sample and Data Processing

We cross-correlated the XMM-Newton RGS and Chandra HRC (Murray et al. 2000) LETG archives with the LLS samples of Lehner et al. (2013) and Prochaska et al. (2019), consisting of 30 quasars observed with the HST-COS crossing LLSs with moderate H I column density ($16.2 \leqslant \log N_{\rm H\ I}$(in cm^{-2}) $\leqslant 19$) and the associated low- and moderate-ionization metal absorbers (Fox et al. 2013; Lehner et al. 2013). We found 11 matches. Seven of these have more than one XMM-Newton RGS public observation, while the remaining four objects have been observed only once and with very short exposures (16–28 ks each) and were removed from the sample. Of the seven targets with multiple RGS spectra (namely, PG 1407+265, PG 1116+215, PG 1216+069, PKS 0312−77, PG 1634+706, PKS 0405−123, and PHL 1811), PG 1216 +069 (total exposure of 100 ks) is a calibration source and was

Table 4
Properties of the X-Ray Spectra of the X-Ray Halo Sample

QSO	LLS	z_{em}[a]	Exposure (ks) RGS1+RGS2	Exposure (ks) LETG	SNRE[b] RGS1+RGS2	SNRE[b] LETG
PG 1407+265	1	0.94	213	NA	4.7	NA
PKS 0405−123	2	0.5726	1402	376	17.2	6.1
PG 1116+215	3	0.1756	776	355	20.9	8.1
			Stacked X-ray Halo Spectrum			
Total and Averages	NA	NA	2391	731	27.5	10.1

Notes.
[a] Redshift of the background quasars.
[b] SNRE at $\lambda_{RF} = 21.6$ Å (in the LLS frame), where the O VII Kα transition lies.

observed several arcminutes off the aimpoint and thus with a severely degraded spectral resolution. This source was also removed from the sample. We downloaded all of the available RGS data of the remaining six targets and reprocessed them with the latest version of the XMM-Newton Science Analysis Software (SAS v. 20.0.0) and calibration to produce a final coadded RGS1+RGS2 spectrum of each target. This was done by first using the SAS tool *rgsproc* with all default parameters except *keepcool* set to no and *witheffectiveareacorrection* set to yes. This produced all standard products, including RGS1 and RGS2 source and background spectra, response matrices, and background light curves. For each observation, the background light curves were checked for background flares caused by high fluxes of soft protons hitting the detectors, normally during the first or last parts of the observations. About half of the RGS observations were contaminated by background flares (a rate of $\geqslant$0.1 counts s^{-1} in the standard background extraction regions) for 3%–5% of their total exposures, and these time intervals were filtered out from the affected observations by rerunning *rgsproc* with nonstandard GTI filters. Finally, spectra of the same target from single RGS1 and RGS2 observations were coadded by using the SAS tool *rgscombine*, which also produces averaged responses for the final coadded spectrum. We checked these coadded source and background spectra of our targets in spectral regions close to the LLS frame O VII Kα transition and verified that source counts largely dominate all spectra in these regions, displaying extraction region–normalized source/background ratios per spectral resolution element of $\lesssim$3.

Two of the six objects of our XMM-Newton sample also have multiple Chandra HRC-LETG observations publicly available. We downloaded these Chandra observations and reprocessed them with the latest version of CIAO (v.4.14; Fruscione et al. 2006) to produce final total LETG spectra of these targets. We did this by first using the standard CIAO script *chandra_repro* on all HRC-LETG observations of our sample to produce negative- and positive-order source and background spectra (and convolved first- to sixth-order effective area × photon redistribution responses; HRC-LETG does not resolve orders) of each observation. The source and background spectra of the same target were then coadded by exploiting the CIAO tool *combine_grating_spectra*.

Finally, we imposed the following two selection criteria on the targets of our sample: (a) that the LLSs detected along their lines of sight have been confidently associated with Milky Way–like galaxies down to sub-L^* luminosities (e.g., Lehner et al. 2013), and (b) that their total RGS and/or LETG spectra have SNRE > 4 in the continuum adjacent the relevant lines, which, in turn, guarantees the use of Poissonian statistics on the data and the $\geqslant$90% sensitivity to O VII Kα absorption lines with LLS frame EW $\gtrsim$10–50 mÅ in the redshift range $z \simeq 0.1$–0.6 (typical of intervening hot CGM Milky Way–like halos in hydrodynamical simulations; e.g., Wijers et al. 2020). The adoption of both criteria guarantees that the signal in the stacked (or simultaneously fit) spectra is not washed out by the absence (either because of no clear galaxy–LLS association or because of the possible intrinsic absence of hot gas associated with the LLS along the particular line of sight) of high-ionization metal X-ray absorption in any of the stacked spectra. Only four targets passed our second selection criterion (namely, PG 1407+265, PKS 0405−123, PG 1116+215, and PG 1216+069), and only three of these four lines of sight (PG 1407+265, PKS 0405−123, and PG 1116+215) intercept LLSs that have been confidently associated with $\sim L^*$ galaxies. For the LLS along the line of sight to PG 1216+069, the closest galaxy down to 0.1 L^* luminosities lies at an impact parameter of 3.2 Mpc from the LLS (Lehner et al. 2013), and the RGS spectrum of this target consistently shows no hint of LLS-associated O VII Kα absorption, suggesting that the LLS along this line of sight is probably imprinted by an intervening Lyα-forest filament rather than the cool CGM of an intervening galaxy (this target was also removed from the LLS sample of Lehner et al. 2013 in their subsequent works; e.g., Berg et al. 2023).

Thus, our final X-ray halo sample consists of three targets with a total of five X-ray spectra: three XMM-Newton RGS and two Chandra LETG.

Table 4 summarizes the properties of the targets of our X-ray halo sample and their X-ray spectra. The last row of Table 4 lists the total available X-ray exposure and SNRE (added in quadrature).

Appendix B
Properties of the LLS and X-Ray Halo

Table 5 lists the properties of the LLS–galaxy associations relevant to this work, namely, the stellar mass M_*, halo mass M_h (defined as M_{200}[14]), and virial radius $R_{vir} = R_{200}$ of the galaxies, together with the impact parameter ρ, the metallicity of the cool CGM in the LLSs, and the column and Doppler parameters of the LLS-associated O VI absorbers.

The virial radii of the galaxy associations are reported in the literature for all three LLSs of our X-ray halo

[14] The mass embedded in a sphere with radius R_{200}.

Table 5
Properties of the LLS and X-Ray Halo

QSO (LLS No.)	z_{LLS}	M_* ($\log M_\odot$)	M_h ($\log M_\odot$)	R_{vir} (kpc)	ρ (kpc)	[X/H]	$\log N_{O\ VI}$ (cm^{-2})	$b_{O\ VI}$ (km s^{-1})
PG 1407+265 (1)	0.6828	10.9[a]	12.4	220[a]	91[a]	−1.66[b]	13.99 ± 0.06[c]	28 ± 10[c]
PKS 0405−123 (2)	0.1672	10.3[d]	11.9[d]	183[d]	117[d]	−0.29[b]	14.59 ± 0.05[c]	78 ± 10[c]
PG 1116+215 (3)	0.1385	10.3[e]	11.9	192[f]	127[g]	−0.56[b]	13.85 ± 0.05[c]	47 ± 10[c]
			X-Ray Halo					
Weighted averages	0.276	10.53	12.1	195	115	−0.512	14.30 ± 0.05	68 ± 10

Notes.
[a] Burchett et al. (2019).
[b] Wotta et al. (2019).
[c] Fox et al. (2013).
[d] Berg et al. (2023).
[e] Assumed to be the same as PKS 0405−123, given the same halo mass.
[f] Keeney et al. (2017).
[g] Lehner et al. (2013).

(Keeney et al. 2017; Burchett et al. 2019; Berg et al. 2023), while the halo mass is reported only for LLS 2 along the sight line to PKS 0405−123 (Berg et al. 2023). For LLS 2, Berg and collaborators estimated M_h via the stellar–halo mass relation, as in Rodríguez-Puebla et al. (2017), and then derived R_{vir} via the relationship $M_h = 4/3\pi R_{vir}^3 \Delta_{200} \rho_c(z)$, where $\rho_c(z) = (3H_0^2/8\pi G)[\Omega_m(1+z)^3 + \Omega_\Lambda]$ is the critical density of the Universe at redshift z. For the other two LLSs, R_{vir} is derived in Keeney et al. (2017) and Burchett et al. (2019) through abundance matching, i.e., via the galaxy's optical luminosity, by matching an observed galaxy luminosity function with a theoretical halo mass function. For these two galaxy associations, we derive M_h from R_{vir}, again as in Berg et al. (2023), through the relationship $M_h = 4/3\pi R_{vir}^3 \Delta_{200} \rho_c(z)$. Finally, the last row of Table 5 lists the properties of the X-ray halo that we use in this work. These are derived (all but the Doppler parameter of O VI, which is further weighted by the column density of O VI) by weighting the quantities in rows 1−3 of Table 5 by the statistical significance of the O VII Kα lines in the spectra of our three targets (i.e., $\sigma^i_{OVII} = 1.7$, 2.8, and 2.8 for PG 1407+265, PKS 0405−123, and PG 1116+215, respectively; Table 1) and averaging them.

Appendix C
Uncertainties in the HRC-LETG and RGS Wavelength Scales

Figure 1 and Table 1 show that the best-fit LLS frame centroids of the putative O VII Kα lines of virtually all of the available RGS and LETG spectra of the X-ray halo are offset from the expected $\lambda = 21.6$ Å position, though for four out of the five spectra, this is by less than the LSF FWHM of the spectrometer (70 and 50 mÅ for the RGS and LETG, respectively). The exception is the line detected at a 2σ confidence level in the HRC-LETG spectrum of PG 1116+215 (made up of 11 different exposures), which is offset by 120 mÅ (i.e., $2.4 \times \mathrm{FWHM_{LETG-LSF}}$) from the line rest-frame wavelength. The same line is seen at a similar statistical confidence level in the RGS spectrum of the same target (1.8σ), and its position is shifted in the same direction but only by 60 mÅ, i.e., $0.86 \times \mathrm{FWHM_{RGS-LSF}}$, from both the line rest-frame position and the centroid of the line in the LETG spectrum.

The large displacement of the line position in the Chandra spectrum of PG 1116+215 could be at least partly due to the large systematic uncertainties that affect the HRC-LETG dispersion relationship. According to the Chandra HRC-LETG calibrations, the wavelength scale of the HRC-LETG spectrometer suffers uncertainties of up to 50 mÅ (about 1000 km s^{-1} at the wavelength of the Fe XVII line, where such an uncertainty has been evaluated) due to the nonlinearity of the dispersion relationship, which, in turn, is due to the nonlinear imaging distortions of the HRC-S detector.[15] Such distortions are randomly spaced in wavelength across the entire spectrum and therefore cannot be calibrated based on the presence of strong lines with known positions in different regions of the same spectrum (which, in any case, are not present in the LETG spectrum of PG 1116+215). Moreover, the 1000 km s^{-1} calibration uncertainty quoted above has been derived for the strong Fe XVII ($\lambda \simeq 15$ Å) emission line of a very bright X-ray star (Capella). The velocity space uncertainty in the aspect reconstruction of the dispersion relation may be larger for fainter lines, especially in absorption against relatively low-flux continua, and could propagate randomly when adding together different low-exposure observations of the same source, with the net effect of shifting the unresolved line centroid even beyond one nominal resolution element.

To investigate this further, we decided to use two samples of absorption lines detected in the X-ray spectra of extragalactic targets, namely, the Galactic O VII Kα and Kβ ($\lambda = 21.6$ and 18.63 Å, respectively) and O I and O II Kα ($\lambda = 23.52$ and 23.35 Å, respectively) lines seen ubiquitously in the spectra of both Galactic and extragalactic targets with sufficient SNRE (Nicastro et al. 2016a, 2016b). The sample of O VII lines is that of Nicastro et al. (2016b), extracted from RGS spectra with SNRE > 10 at 21.6 Å, and contains 34 O VII Kα lines; for 16 of these, the associated Kβ line is also detected. The sample of O I and O II Kα lines is instead that of Nicastro et al. (2016a), extracted from HRC-LETG spectra with SNRE > 3 at 23.5 Å, and contains 11 O I Kα lines; for 10 of these, the associated O II Kα line is also detected. Figure 9 shows the probability density distributions (in bins of 500 km s^{-1}) of the offsets between the best-fitting O VII Kα, Kβ (RGS lines; black solid histogram) and O I, O II Kα (HRC-LETG lines; cyan solid

[15] https://cxc.cfa.harvard.edu/cal/letg/Corrlam/

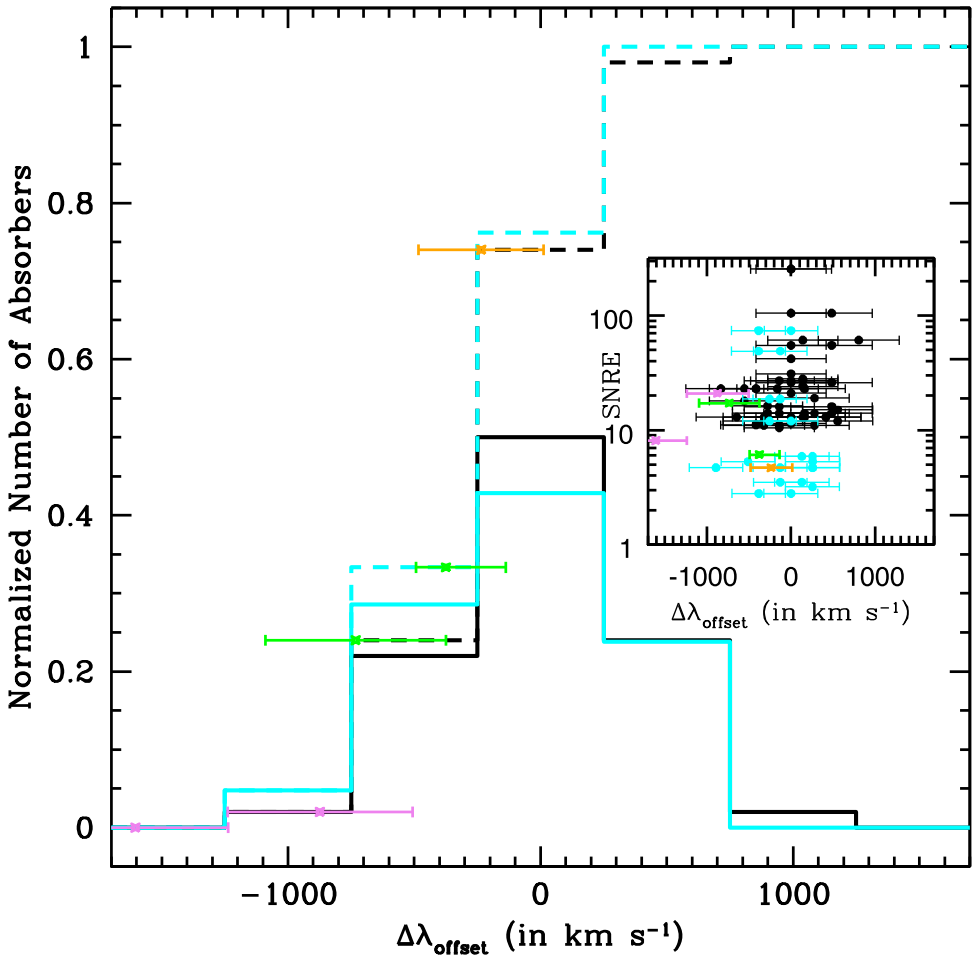

Figure 9. Probability density distributions of the offsets between the best-fitting line centroids of the O VII Kα, Kβ (RGS lines; black solid histogram) and O I, O II Kα (HRC-LETG lines; cyan solid histogram) absorbers from the samples of Nicastro et al. (2016b) and Nicastro et al. (2016a), respectively, and the rest-frame wavelengths of these transitions, together with their cumulative distributions (dashed black and cyan histograms, respectively). The inset shows the single O VII Kα, β (black points and 1σ statistical-only error bars) and O I, O II Kα (cyan points and 1σ statistical-only error bars) line centroid offsets as a function of the SNRE in the spectra.

histogram) line centroids and the rest-frame wavelengths of these transitions, together with their cumulative distributions (dashed black and cyan histograms, respectively). The inset of Figure 9 shows the single O VII Kα, β (black points and 1σ statistical-only error bars) and O I, O II Kα (cyan points and 1σ statistical-only error bars) line centroid offsets as a function of the SNRE in the spectra. Both in the main figure and in the inset, colored points and 1σ statistical-only error bars are the measured O VII Kα LLS frame line centroid offsets in the five spectra of our targets (orange, PG 1407+265; green, PKS 0405 −123; and violet, PG 1116+215).

Both distributions are broad, spanning a range of about 2000 km^{-1} in line centroid offsets, and, in the adopted binning scheme, have $\mathrm{FWHM_{RGS}} \simeq 1000$ and $\mathrm{FWHM_{LETG}} \simeq 1500$ km s^{-1}, about 1× and 2.2× the nominal RGS and LETG LSF FWHMs at $\lambda = 21.6$ Å, respectively. In this paper, we assume, as 1σ (statistical plus systematic) errors for the best-fitting line centroids in the two instruments, the Gaussian-equivalent standard deviation of the distributions, i.e., $\Delta\lambda_{1\sigma} = \pm\mathrm{FWHM}/(2\sqrt{2ln2})$. The centroid of the O VII Kα line in the HRC-LETG spectrum of PG 1116+215 is marginally consistent within its 1σ statistical-only error with both the O VII Kα line seen in the RGS spectrum of the same target (compare the two violet error bars in the main panel of Figure 9) and the negative tail of the observed HRC-LETG O I Kα centroid distribution (sampled with a probability of about 5% in our distribution, i.e., one out of the 21 O I, O II Kα HRC-LETG line centroid measurements; Figure 9).

The breadths of the RGS and LETG line centroid offset distributions are not due to rigid shifts of the dispersion relationship of the two spectrometers from observation to observation. Indeed, these distributions become even broader when the offset between the observed and expected relative positions of two known lines is considered. Figure 10 shows the probability density (solid histograms) and cumulative (dashed histograms) distributions of the offsets (in km s^{-1}) between the O VII Kα, Kβ and O I, O II Kα line centroid differences measured in our RGS (black histograms) and HRC-LETG (cyan histograms) samples, respectively, and the corresponding expected line centroid differences. As in Figure 9, the inset shows the data points from our samples (black from the RGS and cyan from the HRC-LETG) as a function of the SNRE at the relevant wavelengths. Both in the main figure and in the inset, the orange point with its 1σ statistical error bars is the offset between the relative positions of the O VII Kα and Kβ lines measured in the stacked spectrum of the X-ray halo obtained by rigidly shifting each X-ray spectrum to the exact FUV–LLS redshifts (i.e., right panels of

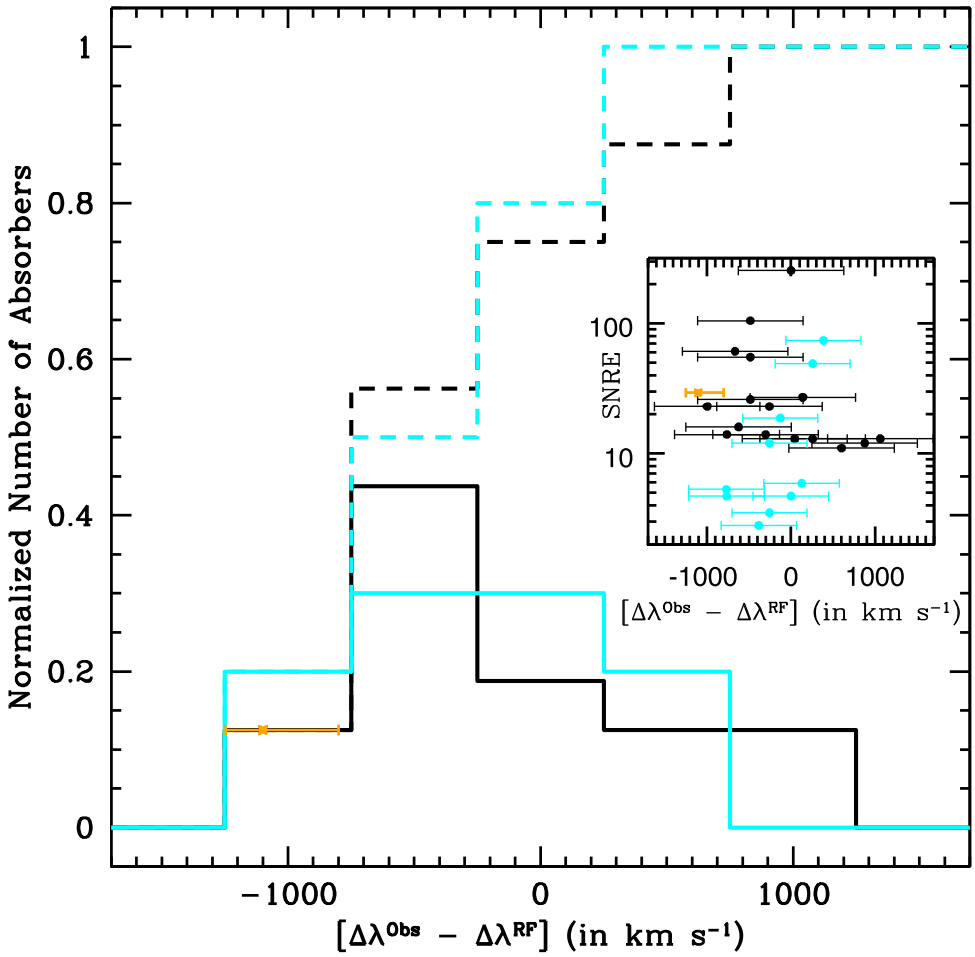

Figure 10. Same as Figure 9 but for the offsets (in km s^{-1}) between the O VII Kα, Kβ and O I, O II Kα line centroid differences measured in our RGS (black histograms) and HRC-LETG (cyan histograms) samples, respectively, and the corresponding expected line centroid differences.

Figures 4 and 5) and their expected relative position. The observed offset is fully consistent with both the RGS and HRC-LETG distributions.

Appendix D
Ion Fractions in CIE and PIE Gas

Figure 11 shows the fractional abundances of the ions O VI (green), O VII (blue), and O VIII (brown) as a function of temperature (left panel) and hydrogen density (right panel) in gas in CIE (left panel) and photoionized by the average metagalactic radiation field at the redshift of the X-ray halo (photoionization equilibrium (PIE); Nicastro et al. 2016a; right panel).

In CIE gas (left panel), O VII is effectively the only populated ion of oxygen at log$T$(in K) $\simeq$ 5.7–6.1 (the virial temperature range for halo masses in the range of $M_h \simeq 10^{11.7-12.3}$ $M_\odot$ at the X-ray halo redshift $z = 0.276$), while the O VI and O VIII fractions peak, respectively, at the opposite extremes of the considered temperature range, namely, log$T$(in K) $\simeq$ 5.5 and T(in K) $\simeq$ 6.4, and reach maximum abundances of only 20% and 40%. Thus, virialized gas in typical L^* galaxy halos can efficiently produce O VII but only small fractions of O VI and O VIII, the first still detectable in the current FUV spectra of bright background targets.

On the contrary, PIE gas illuminated by the metagalactic radiation can produce sizable fractions of O VII only at typical IGM densities ($n_{\rm H} \lesssim 10^{-5.3}$ cm^{-3}), while O VI can still be moderately populated and detectable at typical galaxy halo densities of $n_{\rm H} \simeq 10^{-4}$–10^{-5} cm^{-3}.

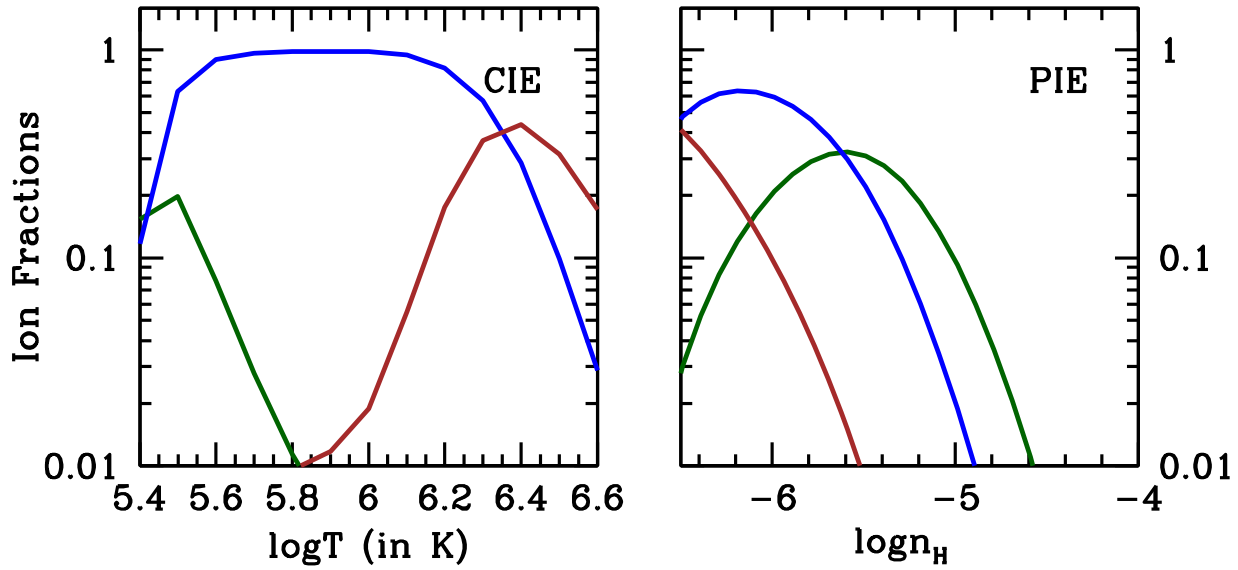

Figure 11. Fractional abundances of O VI (green), O VII (blue), and O VIII (brown) as a function of temperature (left panel) and hydrogen density (right panel) in CIE (left) and PIE gas illuminated by the average metagalactic radiation field at $z = 0.276$ (right).

ORCID iDs

Fabrizio Nicastro https://orcid.org/0000-0002-6896-1364
Y. Krongold https://orcid.org/0000-0001-6291-5239
T. Fang https://orcid.org/0000-0002-2853-3808
F. Fraternali https://orcid.org/0000-0002-0447-3230
S. Mathur https://orcid.org/0000-0002-4822-3559
S. Bianchi https://orcid.org/0000-0002-4622-4240
A. De Rosa https://orcid.org/0000-0001-5668-6863
E. Piconcelli https://orcid.org/0000-0001-9095-2782
L. Zappacosta https://orcid.org/0000-0002-4205-6884
M. Bischetti https://orcid.org/0000-0002-4314-021X
C. Feruglio https://orcid.org/0000-0002-4227-6035
A. Gupta https://orcid.org/0000-0003-1880-1474

References

Afruni, A., Fraternali, F., & Pezzulli, G. 2021, MNRAS, 501, 5575
Ahoranta, J., Finoguenov, A., Bonamente, M., et al. 2021, A&A, 656, A107
Ahoranta, J., Nevalainen, J., Wijers, N., et al. 2020, A&A, 634, A106
Anders, E., & Grevesse, N. 1989, GeCoA, 53, 197
Armillotta, L., Fraternali, F., Werk, J. K., Prochaska, J. X., & Marinacci, F. 2017, MNRAS, 470, 114
Barret, D., Lam Trong, T., den Herder, J.-W., et al. 2018, Proc. SPIE, 10699, 106991G
Berg, M. A., Howk, J. C., Lehner, N., et al. 2019, ApJ, 883, 5
Berg, M. A., Lehner, N., Howk, J. C., et al. 2023, ApJ, 944, 101
Blackburn, J. K. 1995, in ASP Conf. Ser. 77, Astronomical Data Analysis Software and Systems IV, ed. R. A. Shaw, H. E. Payne, & J. J. E. Hayes (San Francisco, CA: ASP), 367
Bregman, J. N., Anderson, M. E., Miller, M. J., et al. 2018, ApJ, 862, 3
Bregman, J. N., Hodges-Kluck, E., Qu, Z., et al. 2022, ApJ, 928, 14
Brinkman, B. C., Gunsing, T., Kaastra, J. S., et al. 2000, Proc. SPIE, 4012, 81
Burchett, J. N., Tripp, T. M., Prochaska, J. X., et al. 2019, ApJL, 877, L20
Cavaliere, A., & Fusco-Femiano, R. 1976, A&A, 49, 137
Chen, H.-W., & Prochaska, J. X. 2000, ApJL, 543, L9
Das, S., Mathur, S., & Gupta, A. 2020, ApJ, 897, 63
den Herder, J.-W., den Boggende, A. J., Branduardi-Raymont, G., et al. 2000, Proc. SPIE, 4012, 102
Fox, A. J., Lehner, N., Tumlinson, J., et al. 2013, ApJ, 778, 187
Fraternali, F. 2017, in Astrophysics and Space Science Library, Gas Accretion onto Galaxies, 430, ed. A. Fox & R. Davé (Berlin: Springer), 323
Fruscione, A., McDowell, J. C., Allen, G. E., et al. 2006, Proc. SPIE, 6270, 62701V
Gehrels, N. 1986, ApJ, 303, 336
Gnat, O., & Sternberg, A. 2007, ApJS, 168, 213
Hafen, Z., Stern, J., Bullock, J., et al. 2022, MNRAS, 514, 5056
Keeney, B. A., Stocke, J. T., Danforth, C. W., et al. 2017, ApJS, 230, 6
Kovács, O. E., Bogdán, Á., Smith, R. K., Kraft, R. P., & Forman, W. R. 2019, ApJ, 872, 83
Lehner, N., Howk, J. C., Tripp, T. M., et al. 2013, ApJ, 770, 138
Lehner, N., Wotta, C. B., Howk, J. C., et al. 2018, ApJ, 866, 33
Lehner, N., Wotta, C. B., Howk, J. C., et al. 2019, ApJ, 887, 5
Mathur, S., Gupta, A., Das, S., Krongold, Y., & Nicastro, F. 2021, ApJ, 908, 69
McGaugh, S. S., Schombert, J. M., de Blok, W. J. G., & Zagursky, M. J. 2010, ApJL, 708, L14
McPhate, J. B., Siegmund, O. H., & Gaines, G. A. 2000, Proc. SPIE, 4139, 25
Moré, J. J. 1978, Lecture Notes in Mathematics, Vol. 630 (Berlin: Springer Verlag), 105
Murray, S. S., Austin, G. K., Chappell, J. H., et al. 2000, Proc. SPIE, 4012, 68
Nicastro, F., Fiore, F., & Matt, G. 1999, ApJ, 517, 108
Nicastro, F., Kaastra, J., Krongold, Y., et al. 2018, Natur, 558, 406
Nicastro, F., Mathur, S., Elvis, M., et al. 2005, ApJ, 629, 700
Nicastro, F., Senatore, F., Gupta, A., et al. 2016a, MNRAS, 457, 676
Nicastro, F., Senatore, F., Krongold, Y., Mathur, S., & Elvis, M. 2016b, ApJL, 828, L12
Nicastro, F., Zezas, A., Drake, J., et al. 2002, ApJ, 573, 157
Prochaska, J. X., Burchett, J. N., Tripp, T. M., et al. 2019, ApJS, 243, 24
Prochaska, J. X., Weiner, B., Chen, H. W., Mulchaey, J., & Cooksey, K. 2011, ApJ, 740, 91
Putman, M. E., Peek, J. E. G., & Joung, M. R. 2012, ARA&A, 50, 491
Planck Collaboration, Aghanim, N., Akrami, Y., et al. 2020, A&A, 641, A6
Qu, Z., & Bregman, J. N. 2018, ApJ, 856, 5
Rodríguez-Puebla, A., Primack, J. R., Avila-Reese, V., & Faber, S. M. 2017, MNRAS, 470, 651
Savage, B. D., Narayanan, A., Wakker, B. P., et al. 2010, ApJ, 719, 1526
Smith, R. K. 2020, Proc. SPIE, 11444, 114442C
Stocke, J. T., Keeney, B. A., Danforth, C. W., et al. 2013, ApJ, 763, 148
Storn, R., & Price, K. 1997, J Glob Optim, 11, 341
Tchernyshyov, K., Werk, J. K., Wilde, M. C., et al. 2022, ApJ, 927, 147
Tumlinson, J., Thom, C., Werk, J. K., et al. 2011, Sci, 334, 948
van de Voort, F., & Schaye, J. 2012, MNRAS, 423, 2991
Werk, J. K., Prochaska, J. X., Thom, C., et al. 2013, ApJS, 204, 17
Werk, J. K., Prochaska, J. X., Tumlinson, J., et al. 2014, ApJ, 792, 8
Wijers, N. A., Schaye, J., & Oppenheimer, B. D. 2020, MNRAS, 498, 574
Wijers, N. A., Schaye, J., Oppenheimer, B. D., Crain, R. A., & Nicastro, F. 2019, MNRAS, 488, 2947
Williams, R. J., Mathur, S., Nicastro, F., et al. 2005, ApJ, 631, 856
Wotta, C. B., Lehner, N., Howk, J. C., et al. 2019, ApJ, 872, 81
Yao, Y., Wang, Q. D., Penton, S. V., et al. 2010, ApJ, 716, 1514